

UNIVERSITY OF PATRAS

DEPARTMENT OF ELECTRICAL AND COMPUTER ENGINEERING

Sector of Telecommunication and Information Theory

Optical Telecommunications

Study of Integrated Photonic Circuits for Optical Telecommunications

D I P L O M A T H E S I S

Dimosthenis Stylios

Ioannis Tomkos

PATRAS – OCTOBER 2022

University of Patras, Department of Electrical and Computer Engineering.

Dimosthenis Stylios

© 2022 – All rights reserved

The whole work is an original work, produced by Dimosthenis Stylios, and does not violate the rights of third parties in any way. If the work contains material which has not been produced by him/her, this is clearly visible and is explicitly mentioned in the text of the work as a product of a third party, noting in a similarly clear way his/her identification data, while at the same time confirming that in case of using original graphics representations, images, graphs, etc., has obtained the unrestricted permission of the copyright holder for the inclusion and subsequent publication of this material.

CERTIFICATION

It is certified that the Diploma Thesis titled

Study of Integrated Photonic Circuits for Optical Telecommunications

of the Department of Electrical and Computer Engineering student

Dimosthenis Stylios

Registration Number: 1059480

was presented publicly at the Department of Electrical and Computer Engineering at

14/10/2022

and was examined by the following examining committee:

Ioannis Tomkos, Professor, Electrical and Computer Engineering

Grigoris Kalivas, Professor, Electrical and Computer Engineering

Michalis Birbas, assoc.Professor, Electrical and Computer Engineering

The Supervisor	The Director of the Division
Ioannis Tomkos	Michael Logothetis
Professor	Professor

ΠΑΝΕΠΙΣΤΗΜΙΟ ΠΑΤΡΩΝ



ΤΜΗΜΑ ΗΛΕΚΤΡΟΛΟΓΩΝ ΜΗΧΑΝΙΚΩΝ ΚΑΙ ΤΕΧΝΟΛΟΓΙΑΣ ΥΠΟΛΟΓΙΣΤΩΝ

ΤΟΜΕΑΣ ΤΗΛΕΠΙΚΟΙΝΩΝΙΩΝ ΚΑΙ ΘΕΩΡΙΑ ΤΗΣ ΠΛΗΡΟΦΟΡΙΑΣ

ΕΡΓΑΣΤΗΡΙΟ ΟΠΤΙΚΩΝ ΕΠΙΚΟΙΝΩΝΙΩΝ

Μελέτη Ολοκληρωμένων Φωτονικών Διατάξεων για Συστημάτων Οπτικών Τηλεπικοινωνιών

Δ Ι Π Λ Ω Μ Α Τ Ι Κ Η Ε Ρ Γ Α Σ Ι Α

ΔΗΜΟΣΘΕΝΗΣ ΣΤΥΛΙΟΣ

ΕΠΙΒΛΕΠΩΝ: Ιωάννης Τόμκος

ΠΑΤΡΑ – Οκτώβριος 2022

Πανεπιστήμιο Πατρών, Τμήμα Ηλεκτρολόγων Μηχανικών και Τεχνολογίας Υπολογιστών.

Δημοσθένης Στύλιος

© 2022– Με την επιφύλαξη παντός δικαιώματος

Το σύνολο της εργασίας αποτελεί πρωτότυπο έργο, παραχθέν από τον Δημοσθένη Στύλιο, και δεν παραβιάζει δικαιώματα τρίτων καθ' οιονδήποτε τρόπο. Αν η εργασία περιέχει υλικό, το οποίο δεν έχει παραχθεί από τον/την ίδιο/α, αυτό είναι ευδιάκριτο και αναφέρεται ρητώς εντός του κειμένου της εργασίας ως προϊόν εργασίας τρίτου, σημειώνοντας με παρομοίως σαφή τρόπο τα στοιχεία ταυτοποίησής του, ενώ παράλληλα βεβαιώνει πως στην περίπτωση χρήσης αυτούσιων γραφικών αναπαραστάσεων, εικόνων, γραφημάτων κ.λπ., έχει λάβει τη χωρίς περιορισμούς άδεια του κατόχου των πνευματικών δικαιωμάτων για την συμπερίληψη και επακόλουθη δημοσίευση του υλικού αυτού.

Department of Electrical and Computer Engineering – Sector of Telecommunication and Information Theory

ΠΙΣΤΟΠΟΙΗΣΗ

Πιστοποιείται ότι η Διπλωματική Εργασία με τίτλο

Μελέτη Ολοκληρωμένων Φωτονικών Διατάξεων για Συστημάτων Οπτικών Τηλεπικοινωνιών

του φοιτητή του Τμήματος Ηλεκτρολόγων Μηχανικών και Τεχνολογίας Υπολογιστών

ΔΗΜΟΣΘΕΝΗΣ ΣΤΥΛΙΟΣ ΤΟΥ **ΧΡΥΣΟΣΤΟΜΟΥ**

Αριθμός Μητρώου: 1059480

Παρουσιάστηκε δημόσια στο Τμήμα Ηλεκτρολόγων Μηχανικών και Τεχνολογίας Υπολογιστών στις

14/10/2022

και εξετάστηκε από την ακόλουθη εξεταστική επιτροπή:

Ιωάννης Τόμκος, Καθηγητής, Ηλεκτρολόγων Μηχανικών και Τεχνολογίας Υπολογιστών

Γρηγόρης Καλύβας, Καθηγητής, Ηλεκτρολόγων Μηχανικών και Τεχνολογίας Υπολογιστών

Μιχάλης Μπίρμπας, Αναπλ.Καθηγητής, Ηλεκτρολόγων Μηχανικών και Τεχνολογίας Υπολογιστών

Ο Επιβλέπων	Ο Διευθυντής του Τομέα
Ιωάννης Τόμκος	Μιχαήλ Λογοθέτης
Καθηγητής	Καθηγητής

PREFACE

The spread of cloud services is driving a relentless increase of traffic demand in large-scale data centers, which is nearly doubling every year. Today, rapidly growing traffic in data centers highlights the urgent need for high-speed low-cost interfaces. This thesis is focusing on the interface of digital to analog converter. Basic part of digital to analog converters is the photonic circuit of modulator. To fulfill today's requirements two aspects have been taken under consideration. The first one is the study of all the ultra-fast modulators in terms of topology (e.g. Mach-Zehnder Modulator (MZM), Electro-Absorption Modulators) and in terms of fabrication techniques. The second one is the design direct digital to optical converter using silicon photonic modulator of inferometric design. By direct digital to optical converters meaning a system capable of transmitting high-rate data from the digital domain directly to the optical domain. This Thesis goal is to verify the theoretical concept of a serial optical digital to analog converter, as this is descripted in 'Perfect' PAM4 serial digital-optical conversion. Then the superior in performance concept of parallel MZM digital to optical converter is explained. Following the successful verification, the study continues with the implementation of newly presented, novel design, optical digital to analog converter, which combines the serial optical digital to analog converter and the parallel one. This architecture can achieve high modulation format (PAM16 and QAM256) only using NRZ drivers. In other words, is a design free of electrical digital to analog converter, which in traditional systems were required so the multilevel signal to be generated and then modulated to the optical domain. The absence of electrical digital to analog converter minimizes the energy demand, the overall complexity but most importantly the system is free of the limitation of an eDAC, usually able only to generate multilevel signals of PAM4.The combination of this presented architecture of parallel with segmented MZM optical digital to analog converter and the ultra-fast modulators described are promising to fulfill the demand of high bit rates of modern intra datacenter telecommunication.

ABSTRACT

Study of Integrated Photonic Circuits for Optical Telecommunications

DIMOSTHENIS STYLIOS **TOMKOS IOANNIS**

The focus of this Thesis is the photonic circuit of modulator. The study of modulators is of great interest since modern telecommunication systems and mainly intra datacenter connection need higher data rates, bigger bandwidth, and lower cost. Central to modern telecommunication systems is the device of digital to analog conversion, in many cases a device costly in power, footprint and with constellation imperfections. In high-speed digital optical transmitters, the Digital to Optical (D/O) translation typically comprises power consuming and costly electrical Digital to Analog Convertors (eDAC)-based data conversion, followed by analogue optical modulation. The idea of adopting a direct Digital to Optical domain (D/O) conversion, eliminating the eDAC intermediaries is put forward, but first a perfect segmented Mach-Zehnder Modulator (SEMZM) must be implemented. Prior to that, the Electro – Optic effects, that offer some materials the ability to modulate light are presented, then the topologies that are in use are explained and the fabrication techniques for different modulators are demonstrated. In the last chapter of this Thesis a silicon Mach-Zehnder Modulator (MZM) and a segmented MZM of the same type are implemented in the simulation tool VPI PHOTONICS. The segmented MZM is acting as an optical Digital to Analog Converter (oDAC) and its performance is studied. Moreover, the multi-level multi parallel oDAC architecture is explained. Finally, a novel design, that combines a parallel modulator's architecture of oDAC and the above segmented MZM is explained and implemented in the VPI Photonics.

ΕΚΤΕΤΑΜΕΝΗ ΕΛΛΗΝΙΚΗ ΠΕΡΙΛΗΨΗ

Μελέτη Ολοκληρωμένων Φωτονικών Διατάξεων για Συστήματα Οπτικών Τηλεπικοινωνιών

Δημοσθένης Στύλος **Ιωάννης Τόμκος**

Η διπλωματική αυτή έχει θέμα την Μελέτη Ολοκληρωμένων Φωτονικών διατάξεων για συστήματα οπτικών τηλεπικοινωνιών. Εστιάζει στην διαμόρφωση του οπτικού σήματος, διότι έχει σαν τελικό στόχο την υλοποίηση μια καινοτόμα αρχιτεκτονικής οπτικού μετατροπέα από ψηφιακό σε αναλογικό σήμα (optical digital to analog converter) . Η σχεδίαση που βασίστηκε στο [9], γίνεται για να επιτευχθούν ψηλότεροι ρυθμοί και ανώτερες τύποι διαμόρφωσης. Στοιχεία τα οποία είναι αναγκαία για το σύγχρονο περιβάλλον τηλεπικοινωνιών, όπου οι ρυθμοί μετάδοσης είναι τεράστιοι και οι διαδικασίες αποθήκευση δεδομένων σε cloud, παροχές stream και το internet of things οδηγούν σε αύξηση του όγκου των δεδομένων. Επειδή το σημερινό περιβάλλον το τηλεπικοινωνίων βασίζεται στο internet του οποίου η ραχοκοκαλιά είναι οι οπτικές ίνες μια φωτονική λύση κρίνεται η πιο δελεαστική. Οι μετατροπείς του ψηφιακού σε αναλογικό σήμα πρέπει να έχουν μεγαλύτερο ήλεκτρο-οπτικό εύρος ζώνης άλλα και την δυνατότητα να κάνουν υψηλού τύπου διαμόρφωσης (PAM, QAM). Συνεπώς πρέπει να μελετηθούν οι διαμορφωτές, τα υλικά και οι αρχιτεκτονικές αυτών που μπορεί να ανταπεξέλθουν στις απαιτήσεις αυτές. Στο επίκεντρο αυτής της μελέτης βρίσκεται η φωτονική διάταξη των διαμορφωτών.

Στο πρώτο κεφάλαιο αυτής της διπλωματικής περιγράφονται όλα τα ήλεκτρο-οπτικά φαινόμενα, τα οποία προσφέρουν σε συγκεκριμένα υλικά την δυνατότητα να διαμορφώνουν το φως. Ως ηλεκτρο-οπτικά φαινόμενα ορίζονται τα φαινόμενα, τα οποία προκαλούν αλλαγές στον δείκτη διάθλασης ενός υλικού λόγω της εφαρμογής ενός εξωτερικού ηλεκτρικού πεδίου. Το ηλεκτρικό πεδίο διαμορφώνει τις οπτικές ιδιότητες του υλικού. Η παρουσία ηλεκτρικού πεδίου επηρεάζει την κίνηση των ηλεκτρονίων στα άτομα ή τα μόρια του υλικού και παραμορφώνει την κρυσταλλική του δομή. Αυτά τα φαινόμενα επηρεάζουν επίσης τις οπτικές ιδιότητες. Πιο

συγκεκριμένα εξετάζεται το φαινόμενο Pockels, το οποίο εμφανίζεται σε κέντρο-συμμετρικού κρυστάλλους, το φαινόμενο Franz-Keldysh, το οποίο εμφανίζεται σε ημιαγωγούς. Επίσης αναλύονται τα φαινόμενο διασποράς ελευθέρων φορέων, το οποίο εξελίσσεται σε υλικά όπου είτε υπάρχει ικανή συγκέντρωση ελευθέρων φορέων είτε δημιουργείται με συγκεκριμένες τεχνικές, αλλά και το φαινόμενο ανάκλασης Bragg.

Στο δεύτερο κεφάλαιο αναλύονται όλες οι γνωστές τοπολογίες διαμορφωτών. Αρχικά αναλύονται οι εξωτερικοί διαμορφωτές, αυτοί δηλαδή στους οποίους εισάγεται το φως μια πηγής laser και το διαμορφώνουν. Ιδιαίτερη έμφαση δίνεται στο διαμορφωτή Mach-Zehnder και όλες τις περιπτώσεις του. Επίσης περιγράφονται οι πιθανές τοπολογίες, οι οποίες μπορούν να χρησιμοποιηθούν για να παραχθεί ένα οπτικό σήμα PAM. Στην συνέχεια αναλύεται ο διαμορφωτής Electro-Absorption, ο οποίος είναι ένας από τους διαδιδομένους και οικονομικούς διαμορφωτές. Τέλος εξηγείται και η διαδικασία απευθείας διαμόρφωσης ένος laser.

Το κεφάλαιο τρία είναι ένα από τα εκτενέστερα κεφάλαια αυτής της διπλωματικής εργασίας, στο οποίο περιγράφεται ο τρόπος κατασκευής και τεχνικές βελτιστοποίηση των πιο γνωστών υλικών που χρησιμοποιούνται. Οι δυο παρακάτω πίνακες συνοψίζουν κατά κάποιο τρόπο το κεφάλαιο.

	EO effect	Topology
LN	Pockels Effect	MZM
III-V SEMICONDUCTORS	Franz-Keldysh StarkEffect/Plasma Dispersion	EAM/MZM
SILICON	Plasma Dispersion	MZM/MRM
ELECTRO-OPT POLYMERS	Τεχνητό Pockels Effect	MZM
TWO DIMENSIONS	Τεχνητό Plasma Dispersion	MZM

	VπL(Vcm)	ER (dB)	EO(GHz)
Hybrid LN-Si	6.7	20	106
LN thin film	0.7	30	100
InP	0.55	25	55
Si MZM	0.62	2.1	17
Si MRM	undefined	8	
Si MZM with Bragg-grating	undefined	3	110
Polymer	0.029	20	15

Στο κεφάλαιο τέσσερα μελετώνται πλατφόρμες, ο οποίες παρουσιάζουν κάποιο ξεχωριστό ενδιαφέρον και γίνεται ανάλυση και παρουσίαση πολλών χαρακτηριστικών τους με κυριότερο την σχέση φάση και τάση. Επίσης κάποιες από αυτές αποτελούν το πραγματικό ισοδύναμο των μοντέλων που υλοποιήθηκαν με χρήση του εργαλείου προσομοιώσεων VPI photonics, που περιγράφεται στο επόμενο κεφάλαιο.

Το κεφάλαιο πέντε αποτελεί πρώτα από όλα το εργαστηριακό σκέλος αυτής της διπλωματικής, κατά το οποίο συγκεκριμένοι διαμορφωτές υλοποιήθηκαν και προσομοιώθηκαν. Επιπλέον αποτελεί την πειραματική επιβεβαίωση του [9], διότι παρουσιάζεται ένας σε σειρά segmented MZM, ο οποίος λειτουργεί σαν οπτικός DAC. Σχεδιάσθηκε βάσει ένος πραγματικού silicon διαμορφωτή και όσων σχετικά με την αρχιτεκτονική του ορίζουν οι συγγραφείς στο [9] και όντως παράγει ένα τέλειο οπτικό σήμα. Επίσης παρουσιάζεται ένα υβριδικό μοντέλο διαμόρφωσης, το οποίο είναι ο συνδυασμός laser άμεσης διαμόρφωσης και ένος εξωτερικού EA διαμορφωτή. Όλα αυτά μπορούν να αποτελέσουν την αρχή για την υλοποίηση παράλληλων αρχιτεκτονικών σαν αυτές που περιγράφονται στο [10] , οι οποίες εν τέλη θα οδηγήσουν σε οπτικούς μετατροπής υψηλών μορφών διαμορφώσεων, οι οποίοι ωστόσο δεν θα χρειάζονται

ηλεκτρικές γεννήτριες PAM. Γεγονός, το οποίο μειώνει την συνθετότατα του συστήματος, το απελευθερώνει από τους περιορισμούς των ηλεκτρονικών συσκευών και το κόστος αυτών.

LIST OF TABLES

Table 1 Optimized parameters of the DML…….page 54

Table 2 Levels of bipolar PAM4 Constellation and Eye Diagram Linearity for ratio =1.25 ……..…..……page 73

Table 3 Levels of bipolar PAM4 Constellation and Eye Diagram Linearity for ratio =1.4 ……..…..……page 73

Table 3 Levels of bipolar PAM4 Constellation and Eye Diagram Linearity for ratio =1.55 ……..…..……page 73

Table 4 Levels of bipolar PAM4 Constellation and Eye Diagram Linearity for ratio =1.7 ……..…..……page 74

Table 5 Levels of bipolar PAM4 Constellation and Eye Diagram Linearity for ratio =1.25 ……..…..……page 74

Table 6 Levels of bipolar PAM4 Constellation and Eye Diagram Linearity for ratio =2 ….……..…..……page 74

LIST OF FIGURES

Figure 1.1 Change of the ellipsoid of Fresnel due to Pockels Effect ……6

Figure 1.2 Plasma dispersion via Electro-optic modulation in integrated photonics…….8

Figure 1.3 Optical Properties of a thin layer of amorphous Si as a function of the real(n) and imaginary (K) parts of the complex refractive index. …….....10

Figure 1.4 Ref 1 Kramer-Kronig Relations…….....10

Figure 1.5 Propagating light in ring resonator structure…….....12

Figure 1.6 Reflection of electromagnetic wave in Bragg Reflector ……13

Figure 1.7 Structures of device with Bragg Grating……14

Figure 2.1 Topology of a simple MZM via internet……15

Figure 2.2 Schematic of PAM-4 using a (a) MZM transmitter using an electric DAC(b) thermometer coded segmented (UWS) MZM transmitter(c) BWS MZM transmitter (d) MRM transmitter using electric DAC and (e) segmented MRM transmitter. Higher-order PAM formats can be achieved using similar configurations,e.g., using three segments in the BWS MZM for PAM-8 via Ref.5……....18

Figure 2.3 Schematic of PAM-4 in (a) AMs in series; (b) AMs in parallel. These topologies work for various kinds of AM such as MZM, MRM and EAM Ref.5…….20

Figure 2.4 Direct NRZ Modulation of a DFB laser via 8 …….....22

Figure 2.5 Distortion of pulse by transient and adiabatic chirp via 8 ……..23

Figure 3.1 Hybrid Si-LN EO Mach-Zehnder modulator. (a) General view showing the un-etched (uniform) LN thin film bonded on top of an MZI written in Si and the

aluminum electrodes. The “SiP Regions” accommodate the Si passive circuitry outside the bonded LN film area. (b) SEM image of the hybrid Si-LN modulator. (c) Composite microscope image (not to scale). DC: directional coupler, PLD: path-length difference, GSG: ground-signal-ground, SiP: Si photonics……....27

Figure 3.2 Electro-optic devices based on etched single-crystal submicron LN thin films. (a,b,c) Monolithically integrated LN modulators in an MZI configuration. Microscope image showing three MZIs with a cross-section schematic (inset). Normalized optical transmission for a 20-mm device versus applied voltage showing a Vp equal to 1:4 V and an ER of 30 dB. EO response for a 5-mm device showing a 3-dB bandwidth of 100 GHz.…….28

Figure 3.3 SEM picture of the InP-based p-i-n junction in a MQW electro-absorption modulator……...32

Figure 3.4 (a) Schematic structure of the transmitter, employing a capacitance-loaded traveling-wave-electrode MZM. (b) Photograph of the fabricated DFB-MZM module (0.5*8 mm2)……..33

Figure 4.1 via M. J. 1. Y. T. 1. B. S. 1. H. S. 1. a. X. W. 1. 2. 3. 4. *. Changhao Han 1, «Ultra-compact silicon modulator with 110 GHz bandwidth » …….45

Figure 4.2 a) The transmission spectrum of the silicon slow light modulator. (b) The EO S21 response of the silicon slow light modulator……..... 46

Figure 4.3 Transmission Schematic and b) Optical eye diagram at 100 Gbps with ER of 3.15 dB. The time scale is 5 ps/div. (c) Optical eye diagram at 112 Gbps with ER of 2.15 dB. The time scale is 10 ps/div…… 47

Figure 4.4 a) SEM picture of the LioniX platform b) Phase shift versus driving voltage……48

Figure 4.5 (A) Top view of an asymmetric Mach-Zehnder interferometer silicon modulator containing two pn junction based phase shifters. The waveguide splitter is an 1x2 multi-mode interference (MMI) coupler. The RF signal is coupled to the travelling wave electrode from the optical input side and termination load is added to the output side. (B) Cross-sectional view of a pn junction waveguide phase shifter in Silicon-On-Insulator. The coplanar waveguide electrode has a signal metal width of ~6 μm and a signal-ground metal separation of ~3 μm. The metal thickness is ~1.5 μm. The high-frequency characteristic impedance of the travelling wave electrode is ~20 Ω. (C) Scanning electron microscope (SEM) image of a pn diode phase shifter waveguide……..... 50

Figure 4.6 The output spectra of a MZI modulator having 3 mm long phase shifters for various voltages applied to one of the arms. The MZI output is normalized to the output of a straight waveguide with the same waveguide length without pn junction and drive voltage. (B) The phase shift of an individual phase shifter vs. the drive voltage for the wavelength round 1550 nm for different phase shifter lengths…….53

Figure 5.1 Implementation of MZM in Vpi photonics……57

Figure 5.2 Inside the phase shifter of the MZM of figure 5.2. ……....57

Figure 5.3 Transmission schematic, ePAM4 driving the MZM of figure 5.1 …….59

Figure 5.4 oPAM4 received after the fiber in the simulation of MZM. ……..60

Figure 5.5 Eye Diagram of the optical pulse of figure 5.4……...61

Figure 5.6 Transmission Simulation of Hybrid DML-EAM signal. ……...62

Figure 5.7 ePAM4 signal that drives the DML-EAM hybrid……..62

Figure 5.8 Generated oPAM4 signal from the DML-EAM Hybrid……63

Figure 5.9 Generated PAM2 signal in case of DML. ……63

Figure 5.10 Phase shifter with two waveguides acting as different segments……66

Figure 5.11 SEMZM that uses the phase shifter of Figure 5.10 ……..67

Figure 5.12 Schematic that simulates the operation of the SEMZM by driving MSB and LSB to each segment of the SEMZM ……69

Figure 5.13 Eye diagram of the received pulse. The levels are equally spaced and are those of a 'perfect' PAM4 ……..70

Figure 5.14 Received Eye Diagram in case that ratio ==1.25 ……70

Figure 5.15 Received Eye Diagram in case that ratio == 1.4……...71

Figure 5.16 Received Eye Diagram in case that ratio ==1.7 ……71

Figure 5.17 Received Eye Diagram in case that ratio == 1.85. ……...72

Figure 5.18 Received Eye Diagram in case that ratio == 2 ……72

Figure 5.19 figure of linearity versus ratio between segment's length……75

Figure 5.19 Transmission Simulation of SEMZM ePAM2 to oPAM4 bipolar coherent detection ……....76

Figure 5.20 Received Optical PAM4 signal of the transmission schematic figure 5.19……..77

Figure 5.21 Perfect Bipolar PAM4 optical signal generated by the transmission schematic figure 5.19……77

Figure 5.22 Schematic of S-way Multi-Level – Driven Multi-Parallel oDAC……78

Figure 5.23 Transmission schematic of parallel oDAC with SEMZM in each arm ……....80

Figure 5.24 Perfect Bipolar PAM 16 optical signal received after the oDAC figure 5.23……...81

METRICS

Extinction Ratio(dB) – Ratio of high-transmission to low-transmission level.

Insertion Losses - measured losses when the transmission level is high transmission the value expected is as low as possible

Electro-optic bandwidth (GHz)- refers to the highest symbol rate, which can be supported.

Optical bandwidth(nm)Suitable wavelength for satisfactory transmission

Footprint(nm*nm) The physical space occupied by the modulator.

Linearity - the coefficient of linear behavior of the device

Driving Voltage (V) - For Phase Modulation is the comparison with halfwave

Energy Consumption(pJ/bit) - The energy lost per bit

Chirp - Abrupt changes in frequency (especially zero chirp)

Contents

LIST OF TABLES XIV

LIST OF FIGURES XV

METRICS XX

INTRODUCTION 1

CHAPTER 1: ELECTROPTIC EFFECTS 4

1.1 POCKELS AND KERR ELECTRO-OPTIC EFFECTS 4

1.2 FRANZ KELDYSH AND QUANTUM-CONFINED STARK 6

1.3 FREE CARRIER EFFECT 6

1.4 PHASE-CHARGE EFFECT 10

1.5 BRAGG EFFECT FOR BRAGG RESONATORS 10

CHAPTER 2: FORMATIVE TOPOLOGIES 14

2.1 MZM 14

2.1.1 Mach-Zehnder Modulator with symmetric coupler and opposite driving voltages 14

2.1.2 Mach-Zehnder Modulator with asymmetric coupler and opposite driving voltages 15

2.1.3 Mach-Zehnder Modulator with asymmetric coupler and arbitrary driving voltages 15

2.1.4 The Travelling Wave MZM (TW-MZM) 15

2.1.5 The Segmented MZM 16

2.1.6 Chirp Factor 17

2.2 MICRORING MODULATORS (MRMS) 18

2.3 DRIVING TOPOLOGIES USING BINARY AMPLITUDE MODULATORS (AMS) 19

2.4 EAM 20

2.5 DML SIGNAL GENERATION 21

2.5.1 DML chirping effects 22

CHAPTER 3: PLATFORMS OF EXTRERNAL CONFIGURATIONS AND DIRECTLY CONFIGURED LASER MATERIAL 24

3.1 LITHIUM NIOBATE 24

3.1.1 The effect of LN in relation to the RF circuit 27

3.2 III-V SEMICONDUCTORS 27

3.3 SILICON 32

3.4 MACH-ZEHNDER SILICON PHOTONIC MODULATON ASSISTED BY PHASE-SHIFTED BRAGG GRATINGS 34

3.5 ELECTRO-OPTIC POLYMERS 35

3.6 TWO-DIMENSIONAL MATERIALS (SILICCON NITRIDE) 36

3.7 PHASE CHANGE MATERIALS 37

3.8 INGAAIAS-BASED MQWS AND PHC 38

CHAPTER 4: CONFIGURATIONS STUDIED 40

4.1 BRAGG FORMATIVE 40

4.1.1 Design 40

4.1.2 Optical and EO bandwidth 41

4.1.3 Information Transmission Capabilities 42

4.2 MODYLATORS SILICON NITRIDE 43

4.3 SILICON MZM 45

4.4 HYBRID MODEL 49

CHAPTER 5: OPTICAL DIGITAL TO ANALOG CONVERTER VPI-PHOTONICS 50

5.1 IMPLEMENTATION OF A SIMPLE MZM 51

5.2 IMPLEMENTATION OF HYBRID SML-EAM MODULE 56

5.3 IMPLEMENTATION OF SILICON PHOTONIC MODULATOR AND INTEGRATION IN NOVEL ODAC DESIGN 58

5.3.1 Serial Segmented MZM acting as oDAC for Direct Detection 59

5.3.1 Serial Segmented MZM performing as oDAC for Coherent Detection ... 69

5.4 IMPLEMENTATION OF PARALLEL ARCHITECTURE OF SEGMENTED MZM 72

CONCLUSIONS 76

REFERENCES 77

INTRODUCTION

The 5G era in wireless communication is increasing the interest in microwave applications in the hundred gigahertz range. Apart from this, there is explosive growth of wireless data traffic, driven by widespread adoption of high-bandwidth services e.g., cloud-storage (Google-Drive) video streaming (Netflix), and machine-to-machine (IoT). To enable the expected transmission rates of hundreds Gb/s, different architectures and platforms are being tested and carrier frequencies in electromagnetic spectrum above hundreds of GHZ. The modern world of communications is based on internet, the backbone of which is composed by optical fibers, ensuring the advantage to the photonic approach by allowing seamless integration with the already existing network. However, this approach, requires optical-to-gigahertz and vice-versa converters with bandwidth of hundreds of GHz, high power handling and linearity. In other words, the need for next generation and higher order optical Digital to Analog Converters(oDAC), that are implemented with photonic integrated circuits (PIC) and more specifically modulators, is here. The topologies, materials and a novel architecture of optical DAC will be discussed in this thesis. Besides the already discussed communications, modulators with high performances would potentially enable many more applications, such as high-speed airborne millimeter-wave photonic relays, agile millimeter-wave communication using photonic frequency conversion, signal distribution for millimeter-wave satellite instrumentation, photonic signal processing of radio signals or millimeter-wave radar, to reach the terahertz frequency range. The main platforms on

which current and future modulators are based is lithium niobate, gallium arsenide, indium phosphide and silicon in different combinations. Some commercially available devices are limited to speeds below 100GHz, but impressive progress can be seen in different studies. In studies considering the optical digital to analog converters research area has pertained to 'serial' Segmented Mach-Zehnder Modulator, based on partitioning the electrodes of the basic Mach-zehnder Modulator (MZM). Alternative parallel oDAC approaches mainly addressed the Direct Detection use-case. In this thesis an new optical PAM generation concept is presented.Before implementing the novel design oDAC, the principles and topologies of the modulator must be understood. In the first chapter of this thesis are explained the electro-optic (EO) effects, which provide the necessary change in the optical properties of certain materials when subjected to electric fields of frequency substantially below that of the light wave. Modulators are implemented with materials, whose optical properties can be changed by applied electric field. The topologies that are in use are descripted in chapter two, and how the applied electric field, in other words the voltage, can modulate the light is given by mathematical expressions. In chapter three the most common materials and the fabrication techniques in use of creating modulators are explained. The materials used in modulators are categorized in chapter three. Moreover, is explained how different fabrication techniques can create modulators with higher performances. The main metrics that are taken under consideration for each modulator are the $V\pi L$, the extinction of ratio and the EO bandwidth. In chapter four, some of the recently presented in literature modulators are studied. Final in chapter five a silicon MZM is implemented and is used as the basic of the further analysis. Then a hybrid modulator is implemented, using a direct modulated laser and EAM to modulate the

signal and minimize the chirp. Both of this are in need of a eDAC, that will firstly generate the multilevel (PAM 4) signal and then this signal is modulated in the optical domain. In section 5.3 is implemented for the first time the theoretical concept of a serial optical DAC using a silicon modulator. The study continues with verifying of the perfect constellation of the serial oDAC as those described in 'Perfect' PAM4 serial digital-optical conversion. Following the successful verification, the study continues with explaining a better architecture for the oDAC, that of the parallel MZM. The innovation of this thesis is implementing the parallel oDAC using segmented MZM in each arm, which act as serial oDACs. This novel architecture as presented here can generate an optical PAM16 signal using only digital NRZ signal.

CHAPTER 1: ELECTROPTIC EFFECTS

To achieve modulation of the optical signal, electro optic effects must be understood. Electro optic effect refer to changes in the refractive index of a material that are created due to the application of an external electric field. The electric field shapes the visual properties of the material. The presence of an electric field affects the movement of electrons in the atoms or molecules of the material and deforms its crystalline structure. This effect also affects the visual properties. For example, an applied external field can make a visually isotropic crystal such as GaAs become double chambered. That is, it acquires two refractive indices, usually, the changes in the refractive index are small. The frequency of the applied field must be such that, in the time it takes for the properties of the medium to change (in other words for the medium to respond), as well as for a beam of light to cross the material, the field is considered static. Electro optic phenomena are divided into first and second-order phenomena. [1]

1.1 POCKELS AND KERR ELECTRO-OPTIC EFFECTS

Pockels effect is linear effect present on modulators, which are implemented in crystals with a specific symmetry like LiNbO3. More of modulator's platforms are discussed in chapter 3.

If we consider the refractive index n as dependent on an applied electric field E, that is, if n = n(E), we can write the Taylor spread of this relation:

$$n' = n + a^1 E + a^2 E^2 + \dots (1)$$

The coefficients a^1 a^2 are the linear electro optic phenomenon and the coefficient for the second order electro optic phenomenon, respectively. Longer conditions of the spread do not contribute to the phenomena. The change in a^1 a^2, because of the first term in the spread (of the term) is called the Pockels effect. The change of n because of the second term, is called the Kerr effect. The constant is generally written λK, K is called the a^2 coefficient Kerr. So

$$Dn = a^1 E\ (2) \quad \text{and} \quad n = a^2 E^2 = (\lambda K) E^2 (3)$$

Only some crystalline materials present the Pockels effect in contrast to all materials present the KERR effect. More specifically only in crystals that are non-centrosymmetric, does the Pockels effect occurs. Dn should also be changed i.e., a different field must be created according to the direction of the field. So far, a simplified description of the Pockels effect was good enough to make understood the effect. However, the effect of a field applied to a specific direction of the crystal on the refractive index when the light is polarized and has a specific transmission direction has not been considered yet. Due to the Pockels effect the field will change the ellipsoids of Fresnel. As an example, consider a crystal of LiNbO3 figure1.1:

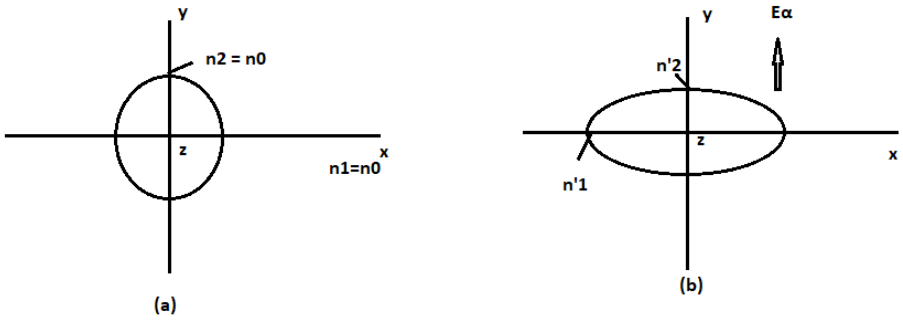


Figure 3.1 Change of the ellipsoid of Fresnel due to Pockels Effect

The wave is transmitted to the z-axis and will face the same refractive index (n1=n2=n0), whatever the polarization. Therefore, the applied field creates, for the light transmitted in the direction z, the applied field creates a refractiveness. According to the Pockels effect the new refractive indicators n1' and n2' are:

$$n'1 \sim n1 + \frac{1}{2} n1^3 r_{22} Ea \ (3) \ , \ n'2 \sim n2 + \frac{1}{2} n2^3 r_{22} Ea \ (4)$$

The coefficient r_{22} being constant, called the Pockels coefficient. More specifically the electro optic reaction to the Pockels effect is described by the coefficients, which define the third-order linear rijk tensor's equation (27 elements), of which 18 are independent. These are placed in a table of 6 * 3, using a standard reduction of indicators, some of them will end up being 0, due to symmetry of the crystal. In the above example of LiNbO3 crystal the independent coefficients are

4 [r33, r13, r22, r51] and when the external electric field is aligned with the optical axis, the crystal remains uniaxial, and the original axes are preserved. The most effective configuration for phase modulation is the transverse modulator, with the optical wave propagating on the x axis and polarizing mainly on the z-axis, while the external electric filter causing a change in the indicator through r33, which is parallel to the z axis.

It is obvious that the control of the refractive index by an externally applied field (and therefore by a voltage) is a separate advantage that allows the formation and control of the phase change through a crystal Pockels. Such a phase modulator is called the Pockels cell. All in all, the applied field is perpendicular to the direction of light transmission.

1.2 FRANZ KELDYSH AND QUANTUM-CONFINED STARK

The Stark effect describes the behavior of some materials, in which the application of an electric field to atoms and molecules shifts the energy state, by changing the energy of electrons.

The Franz Keldysh effect is present in semiconductors. Specifically in bulky semiconductors or isolators, the field effect leads to tilting of the energy amplitude at its edges. Now the electron-hole wave function near the conduction band does not correspond to a simple wave but is described by Airy functions. As a result, they expand into the void exponentially, occupying previously forbidden zones. The phenomenon can be described as a light-assisted tunneling process. Franz Keldysh depends on the size of the crystal. Electrons and holes are confined in three-dimensional one-dimensional potential lattices in nano-level structures [2].

1.3 FREE CARRIER EFFECT

One of the most promising platforms in the modulator's world is the Plasmonics. These devices based on the behavior of the free carriers of the material. The phenomenon of free vectors, also known as the plasma dispersion effect, refers to the dependence of visual properties (both optical refraction and absorption) on the concentration of free carriers. It occurs in semiconductors and

semimetals. Changes in the concentration of free agents affects the optical absorption of the material, but also the dielectric constant of the material is affected, as defined by the Krammers-Kronig relationship. Thus, it becomes permissible to control both the amplitude and phase of the driven wave. Dispersion of carriers accelerates reverse-biased p-n junction.

The technique that achieves the highest configuration speed is the one that uses the plasma-dispersion effect, where changes in the concentration of free electrons and holes leads to a change in the refractive index of the material and the absorption of the material. The density of the carrier, including diode-like architectures, changes as in figure 1.2:

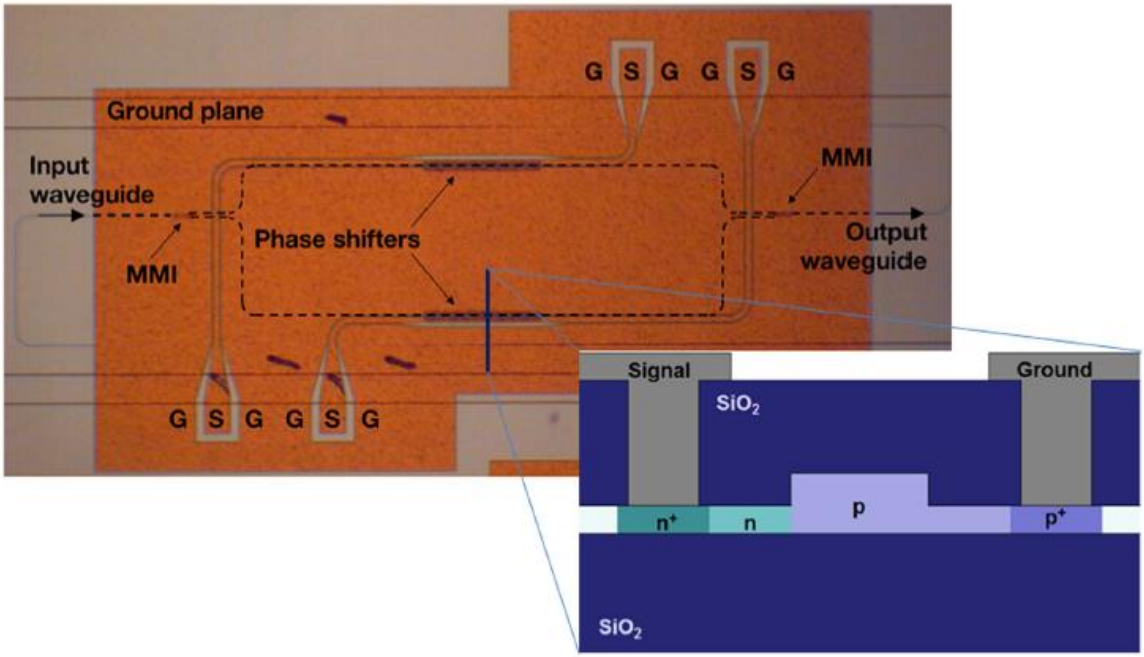


Figure 1.2 Plasma dispersion via Electro-optic modulation in integrated photonics

Depletion and accumulation of the carrier were included in the carrier manipulation techniques, which reach speeds of 50Gb/s compared to the few tens of Mb/s offered by the injection technique. In more detail an electromagnetic wave $E = Eo\, expj(\omega t - kz)$ (5), travelling in a medium, dampens due to absorption, which can be described by a complex constant of propagation *k*:

$$k = k' - jk'' \ (6)$$

where k' it is the true and k'' complex part. If we insert them into the wave function, then we have:

$$E = Eoexp(-k''z),\ expj(\omega t - k'z) \ (7)$$

The amplitude decreases exponentially as the wave propagates on the axis z. The true part k' of the complex propagation constant described the propagation characteristic *e.g.*

$$phase\ velocity\ v = \omega/k \ (8)$$

While the imaginary part k''describes the damping rate on the z-axis. Where I is propagaating at the z-axis:

$$\mathrm{I} \propto |E|^2 \exp(-2k''z)\exp(-2k"z) \ (9)$$

Therefore, the rate in the intensity function of the distance is $\frac{dz}{dI} = -2k''I \ (10)$, where the negative sign represents the damping. Considering it k_o as the propagation constant of the vacuum. This is a true number, since a simple wave does not suffer any loss in free space. The complex refractive index N with real part n and imaginary K, is defined as the percentage of complex constant propagation in a medium to the constant propagation in free space,

$$N = n - jk = \frac{k}{ko} = (ko) * [k' - jk''] \ (11)$$

$$n = \frac{k'}{k_o} \ (12)\ ,\ k = \frac{k''}{k_o} \ (13)$$

The actual part n is called the refractive index while the imaginary part K is called the damping coefficient. When there is no attenuation, the equation is written as following:

$$k" = 0$$

$$k = k'$$

$$N = n = \frac{k}{k_o} = \frac{k'}{k_o}$$

Knowing that when there are no losses, the relationship between the refractive index n and the relative permeability is $n = \sqrt{\varepsilon_r} \ (14)$.Now 11 becomes

$$\mathrm{N} = n - jk = N = n - jk = \sqrt{\varepsilon_r} = \sqrt{\varepsilon_r' - j\varepsilon_r''} \ (15)$$

When the energy of the photons is less than the energy gap, k is negligible, and n is close to 3.5. On the other hand, when the energy of the photons grows, and especially when it exceeds the energy gap, n and K change dramatically as shown in Figure 1.3.

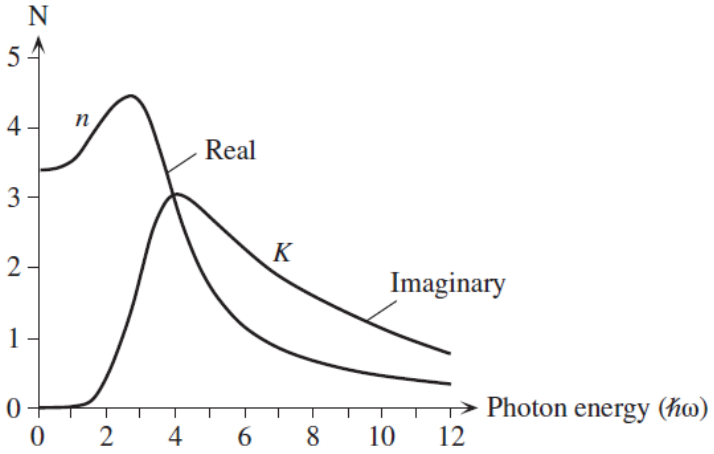


Figure 1.3 ***Optical Properties of a thin layer of amorphous Si as a function of the real(n) and imaginary (K) parts of the complex refractive index.***

The relations that connect the real with the imaginary part of the relative permeability are called Kramer-Kronig. If the dependence of the real and the imaginary part on frequency is $\varepsilon_r'(\omega)$ and $\varepsilon_r''(\omega)$, then the one function can be determined by the other figure 1.4.

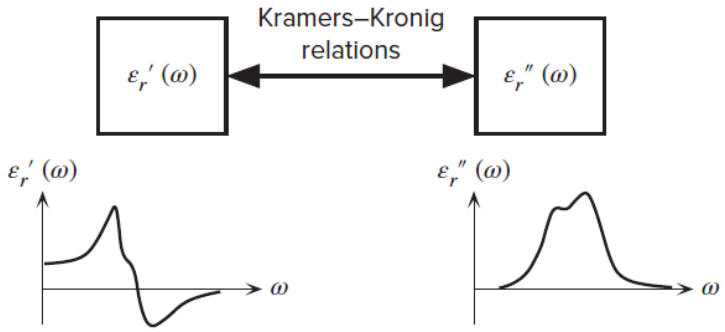


Figure 1.4 Ref 1 Kramerd-Kronig Relations

The optical properties n and K can be calculated by measuring the reflectivity of the surface of the material as a function of polarization and angle of incidence based on Fresnel equations.

1.4 PHASE-CHARGE EFFECT

Phase change materials are those, that can experience phase transition, as a reaction to external stimuli (temperature, electric field, optical illumination). They are mainly classified as Transition metal oxide Chalcogen-based alloys. In the first category classify metal oxide, which are suspected of inversion crystalline- to-crystalline (electronic) transition which are suitable for amplitude phase shaping and routing. Materials, which undergo an amorphous-to-crystalline (structural) transition and are primarily exploited for non-volatile applications, such as memory operation, are called Chalcogen-based alloys. For modulation platforms, their ability to change phase electrically is the one that matters.

1.5 BRAGG EFFECT FOR BRAGG RESONATORS

Resonators are a key building block for many optical devices to name same: add/drop multiplexers, modulators, and delay lines. Optical fibers and circular resonators are based in the principal of reflection of light inside the media, but not exactly in the same way. The fact that in an optical fiber the refractive index is greater within the channel than in the surrounding material and thus the light is limited and travels within the fiber, sounds like an easy solution to apply the same method for the resonator. It is also known that huge leaks occur when a fiber is bend, so implementing a circular fiber and waiting to act as a resonator is bad idea. To solve these problem circular boundary conditions are being used. To satisfy the circular boundary conditions figure1.5, the field in the resonator must satisfy the phase condition, which defines the wavelength that can be propagated [3]:

$$\frac{\lambda_m}{n} = \frac{2\Pi R}{m} \quad (16)$$

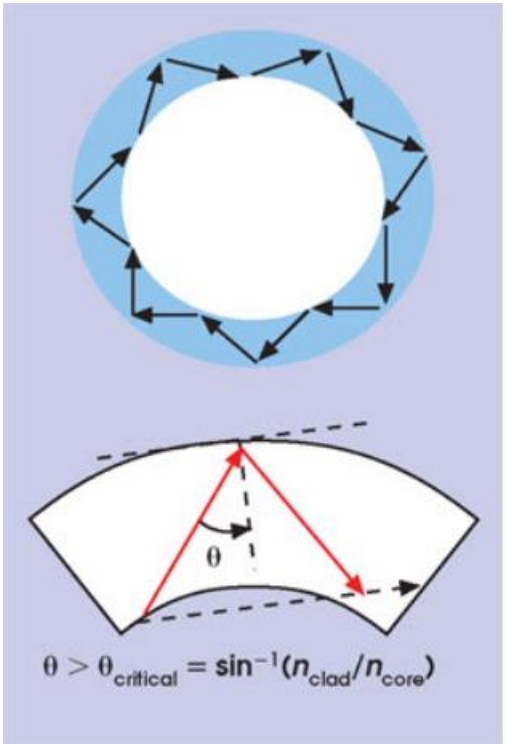


Figure 1.5 Propagating light in ring resonator structure

As it becomes clearer optical fibers and conventional circular resonators may employ the same method of constraint, they are totally different due to the bending of the waveguides. The incident wave is fully reflected by total internal reflection only when the interfaces are straight. For a circular moderator, the interfaces are bent, the reflection is incomplete and part of the light in the guidance channel leaks into the lining, which leads to a constant loss of power from the waveguide. This loss mechanism, called bending, is inherent in the curved geometry of the waveguide. Bending losses depend mainly on the contrast of the refractive index between the core and the lining and on the bending radius, where a lower indicator contrast and a smaller bending radius result in greater losses. For real applications, low levels of losses and high levels of Q factor are required. With the use of a classical resonator there is a permanent tradeoff between an increase in the refractive index and the scattering losses that it causes. It is not limited either by the structure or by the refractive index, nor is a base angle defined, because the periodic structure can be specifically designed to effectively reflect any wavelength. In an ideal Bragg reflector applies $d_i =$

$\frac{\lambda}{4n_i}$ Such a structure ensures that individual reflections from the interfaces separating (figure 1.6) the successive layers accumulate the same phase (up to an integer multiple of 2P) and, therefore, by interfering constructively, high reflectivity is attributed.

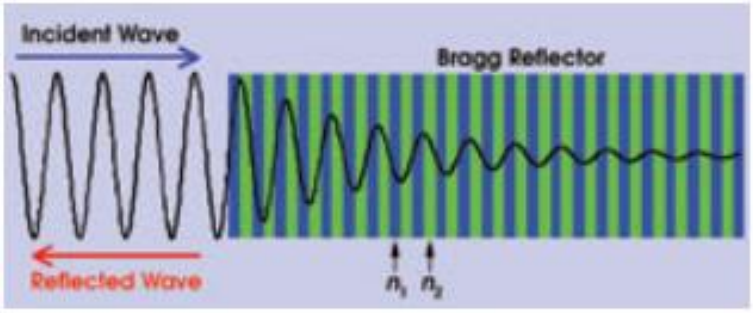


Figure 1.6 Reflection of electromagnetic wave in Bragg Reflector

In the traditional Bragg reflector, waves that propagate forward and backward or are stagnant are superimposed, as shown in figure 1.6. The amplitude of the wave decreases exponentially in the reflection area, depending on whether the wave is transmitted at the front or the rear part. The layers are placed so that they achieve an exponential decrease or increase in width, depending on which type of indicator is placed in the ventricles and on which ones in the bonds. In figure 1.6 the sides of the areas have a magnitude of 1/4 of the wavelength wave, which is why we have this effect. Although there is no equivalent Bloch theorem for circular coordinates, it can be understood based on the above, that a Bragg resonator with circular dimensions can be designed, that is, by placing the walls in the ventricles and bonds of the wave.

Conventional and circular Bragg resonators have many similarities. In both cases, the layers have a thickness equal to 1/4. If the concept of "fourth of the wavelength" is associated with the distance between one-zero and the next end of the wave. i.e., sin or cos. In circular geometry, where the Hankel Bessel functions whose solutions are applied nonperiodically, the widths of the Bragg layers vary depending on the Bessel/Hankel oscillations. The design is done very carefully and is that of figure 1.6.

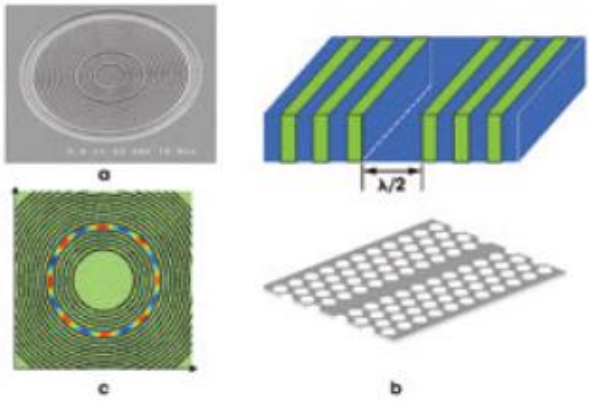


Figure 1.7 Structures of device with Bragg Grating

The mechanism of guidance of the electromagnetic wave is like that of a Cartesian waveguide Bragg, photonic crystal. In a Bragg ring the waves that are propagated are replaced by radial outgoing and incoming waves, which obey the Hankel functions of the first and second species.

CHAPTER 2: FORMATIVE TOPOLOGIES

2.1 MZM

The first and most important topology, that is referenced in this thesis is Mach-Zehnder Modulator. The nature of this device is to modulate the phase of the propagating light. That is achieved by its interferometric structure as shown in figure 2.1, which is implanted with a materials, in which electro optic effects are present. Consequently, applying an external electric field to the arms of the mzm changes optical path lengths resulting in phase modulation, as discussed in chapter1. In reference [4]

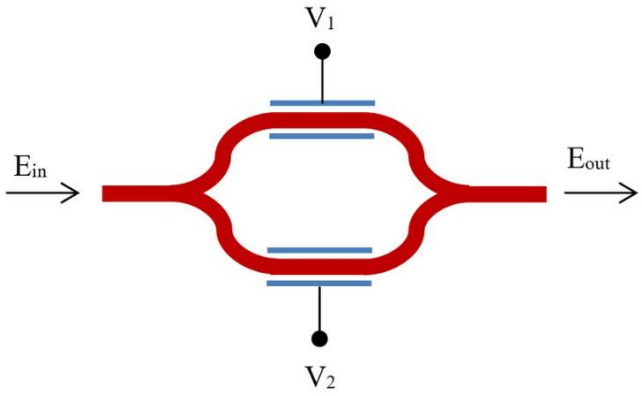


Figure 4.1 Topology of a simple MZM via internet

2.1.1 Mach-Zehnder Modulator with symmetric coupler and opposite driving voltages

Looking in Figure 2.1 and assuming that the input optical field is equally split between the upper and lower arms, and that the voltages driving the phase shifters are opposite $V_2 = -V_1$ the equation that described E_{out} as function of E_{in} is

$$E_{out} = E_{in} \cos \frac{\pi * V_1}{2 * V_\pi} \quad (17)$$

2.1.2 Mach-Zehnder Modulator with asymmetric coupler and opposite driving voltages

For the assumption that the input optical field is not equally split as previously, but the voltages driving the phase shifter are still opposite, the characteristic equation of the output optical signal is:

$$E_{out} = E_{in}\left(\cos\frac{\pi * V_1}{2 * V_\pi} - \mathrm{j}k * \sin\frac{\pi * V_1}{2 * V_\pi}\right) \quad (18)$$

The *k* factor is created so the imbalances to be taken under consideration also results in the appearance of the extinction ratio. Specifically for the Mach-Zehnder modulator the extinction ratio can directly defined from the *k* factor as:

$$ER = \frac{1}{K} \quad (19)$$

In case the extinction ratio is not ideally infinite the imaginary *j* factor component of the equation represents the spurious phase shift that appears.

2.1.3 Mach-Zehnder Modulator with asymmetric coupler and arbitrary driving voltages

This is the most generic case of Mach-Zehnder Modulator, and the characteristic equation of output optical signal is written as:

$$E_{out} = E_{in}\left(\cos\frac{\pi * V_D}{2 * V_\pi} - \mathrm{j}k * \sin\frac{\pi * V_D}{2 * V_\pi}\right)e^{j\frac{\pi V_S}{2V_\pi}} \quad (20)$$

In the equation it is defined the difference of electrical inputs as VD and their average price as Vs.

$$V_{D=\frac{V_1-V_2}{2}} \quad (21)$$

$$V_{S=\frac{V_1+V_2}{2}} \quad (22)$$

2.1.4 The Travelling Wave MZM (TW-MZM)

A travelling wave electrode is integrated in the phase shifters of the device, to allow co-propagation of electrical (RF signal) and optical. Achieving in this way a better tradeoff between the efficiency

and bandwidth of the modulator. An implementation of which has been done as part of this Thesis, using the simulation tool VPI-Photonics.

2.1.5 The Segmented MZM

The conventional method for generating optical PAM signals, is to firstly generate the multilevel in the electrical domain and then modulated it. To reduce the cost of electronic DAC and to reduce the complexity, it was proposed to create the so-called segmented MZM. This device has a concentrated structure and is effective in terms of power. It has a large electro-optical bandwidth and is more efficient in configuring, it is called segmented MZM, because the original structure is segmented into a structure with several electrode, each of which receives a separate on-off keying (OOK) data stream, as in figure 2.2b.

We have two topologies of this kind:

- unary-weighted segmentation (thermometer-coded segmentation)
- weighted binary codes to determine the length of each segment

The implementation with thermometric code is done with the use of a segmented MZM with equal length sections (figure 2.2(b)). Then several low-power distributed amplifiers can be used to drive a long segmented optical phase shifter. Delay between amplifiers can be synchronized using Travelling Waveguides transmission lines and digital delay control blocks. In such a scheme, binary inputs can be applied directly to RF drivers for a minimized number of segments, simplifying the driving configuration. as it is the largest. Binary coding can also be applied to a uniform segmentation design, where several segments can be grouped to receive the same bit stream. In this case, the weight of each group of sections is determined simply by the number of sections. Despite the excessive complexity in electrical connections and latency control, both segmentation topologies help limit voltage swing, allowing the use of low-power CMOS drive circuits.

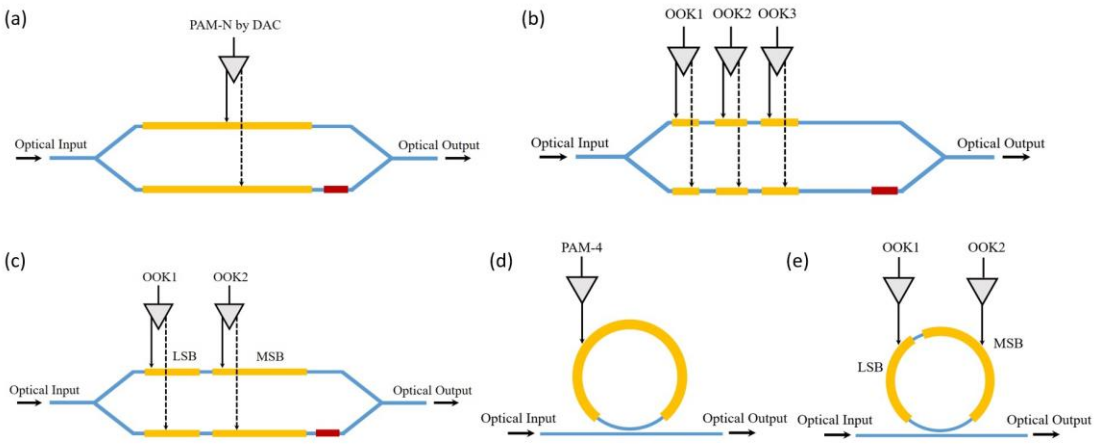


Figure 2.2 Schematic of PAM-4 using a (a) MZM transmitter using an electric DAC(b) thermometer coded segmented (UWS) MZM transmitter(c) BWS MZM transmitter (d) MRM transmitter using electric DAC and (e) segmented MRM transmitter. Higher-order PAM formats can be achieved using similar configurations, e.g., using three segments in the BWS MZM for PAM-8 via Ref.5.

2.1.6 Chirp Factor

Although in terms of Chirp MZM are considered as ideal devices. In case of an ideal MZM, with perfect power split between arms and opposite voltages the chirp factor can even be assumed equal to zero. Generally, MZMs in push-pull operation have very low chirp. In the reference article the chirp factor is defined by the following equation as a function of output frequency and amplitude modulation.

$$a = \frac{\frac{d\theta}{dt}}{\frac{1}{E_{out}}\frac{dEout}{dt}} \quad (23)$$

The circuital behavior of an MZM depicted as External Modulator is shown in Figure 2.2 The dependance on the design and platform it was based on is very high. A good design has a high ER with a small chirp, which requires high levels of driving voltage.

2.2 MICRORING MODULATORS (MRMS)

An equally popular solution for integrated transmitters is the micro ring modulators (MRM). They are characterized by excessively low power consumption. Additionally, they are the most concentrated topology. They are ideal for optical intercom and high-density range communication at the chip level. However, they are particularly sensitive to friction and temperature changes, so heaters and feedback controllers are required to lock the resonant wavelength. They can be driven like an MZM by a very flat electrical signal resulting from a DAC. It of non-importance the levels of electrical signal generated using a DAC, meaning they are functionally perfect form multilevel ePAM signals as shown in figure2.2(d). So, a phase shifter is inserted in the ring cavity for intra-cavity modulation. The output amplitude depends on the round-trip phase of the cavity, specifically the radius of the ring. Due to the strong optical field built up in the cavity near the resonant wavelength, the modulation efficiency can be significantly enhanced compared to MZM. Moreover, an MRM can selectively modulate a single WDM channel, enabling a multi-channel WDM transmitter without requiring an extra wavelength multiplexer. One or a pair of MRMs can be inserted in the MZI arms for a compact MZM, namely, an RA-MZI modulator that offers better linearity and chirp performance compared to single MRMs. Amplitude modulation of an MRM can also be achieved by modulating the coupling between the microring cavity and the bus waveguide. Another resonant structure, such as integrated Bragg grating, can be used to make SiP more compact and increase their frequency and bandwidth of operation.

2.3 DRIVING TOPOLOGIES USING BINARY AMPLITUDE MODULATORS (AMS)

In the above architectures, the PAM optical signal is achieved, through phase configuration and visual interference or resonance. However, a PAM optical signal can also be achieved by combining several binary width modulators.

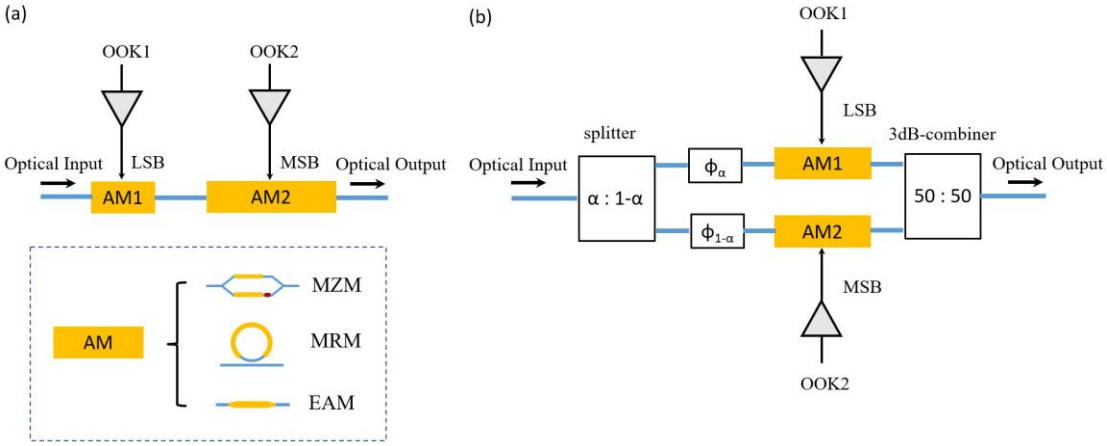


Figure 2.3 Schematic of PAM-4 in (a) AMs in series; (b) AMs in parallel. These topologies work for various kinds of AM such as MZM, MRM and EAM Ref.5.

Figure 2.3 demonstrates two architectures for PAM-4. The first one consists of two AMs in series connection, which are driven by 2 independent NRZ drivers. While the other architecture is designed with two AM in parallel connectivity, an AM can be either MZM, MRM, or electro-absorption modulator (EAM)

In the series architecture, the response of the PAM modulator is the result of the product of the transport function of each AM. As can be seen, each produces a separate OMA: one denotes MSB and the other LSB. And as it is obvious the final signal suffers from the insertion loss of each AM. In the parallel architecture, figure 2.3(b), the response of the PAM modulator is the vector addition of the transport function of each AM. It consists of one power separator, two identical EAM, phase shifter DC and 3 dB combiner. By synchronizing the percentage of power, shared between the two branches, one EAMs acts as an MSB, and the other as an LSB, for the same

driving voltage value. The dc phase shifter between the two branches provides an extra degree of freedom to place the PAM-4 levels at an equal distance.

2.4 EAM

As stated in [8] the EAM is considered an ideal configurator for high-speed optical communication, due to the small driving voltage, large bandwidth, high modulation efficiency and the possible monolithic integration with other semiconductor devices. This device function as an intensity modulator that changes the absorption properties of the carrier optical signal through the application of voltage V(t) around the band edge of the waveguides. Unlike an MZM, which modulates both the intensity and phase of the alleged signal, the EAM as an intensity modulator, has additional advantages, e.g., its linearity in higher order modulation formats, which offers a lower total harmonic distortion compared to the MZM. In contrast, the MZM can achieve higher ER levels, for an EAM to achieve a similar ER, it would be required to increase the size, and therefore result in a large increase in IL. In terms of driving an EAM, a negative polarization voltage guarantees effective light absorption of the modulator. In chapter 3 the characteristic operating curve of the EAM is shown, for bias Voltage [-4V to 1V] and the power obtained at the output.

The polarization of the modulator must be maintained within the linear area to avoid signal distortion. However, in this case, the voltage polarization shows a compensation between the efficiency of the configuration (opening in the eye-diagram) and the limits of the linearity of the EAM. Increasing the amplitude would achieve a widening of the linear area of the EAM. Something like that, of course, would have the direct negative consequence of the reduction of the quality of the distorted eye signal. In the designing and fabrication of an electro-absorption modulator there are two main options: i) The bulk process, which is based on the Franz-Keldysh Effect, and ii) The Multi-Quantum Well (MQW), which is based on the Quantum Confined Stack Effect (QCSE). Specifically, as far as EAMs-based on GeSi are concerned, they have a smaller footprint and less power consumption of MZMs, but also a larger optical range of MRMs.

Operating range for Ge EAMs is the L-band (around 1600nm) and can of course be shifted to the C-band (1550 nm) by introducing Si. However, at these wavelengths there is increased color dispersion. In order not to limit maximal fiber span, hedging techniques are required.

2.5 DML SIGNAL GENERATION

In this topology an electrical signal penetrates directly into the laser cavity in order to manipulate the excited emission present in the laser cavity. In this way, a high-frequency electromagnetic signal with information could be sent via optical channel after modulation. The presence of high chirp is the major disadvantage of this topology and should be mentioned, figure 2.4 gives an illustration of how the DML approach can be achieved and its chirp effects.

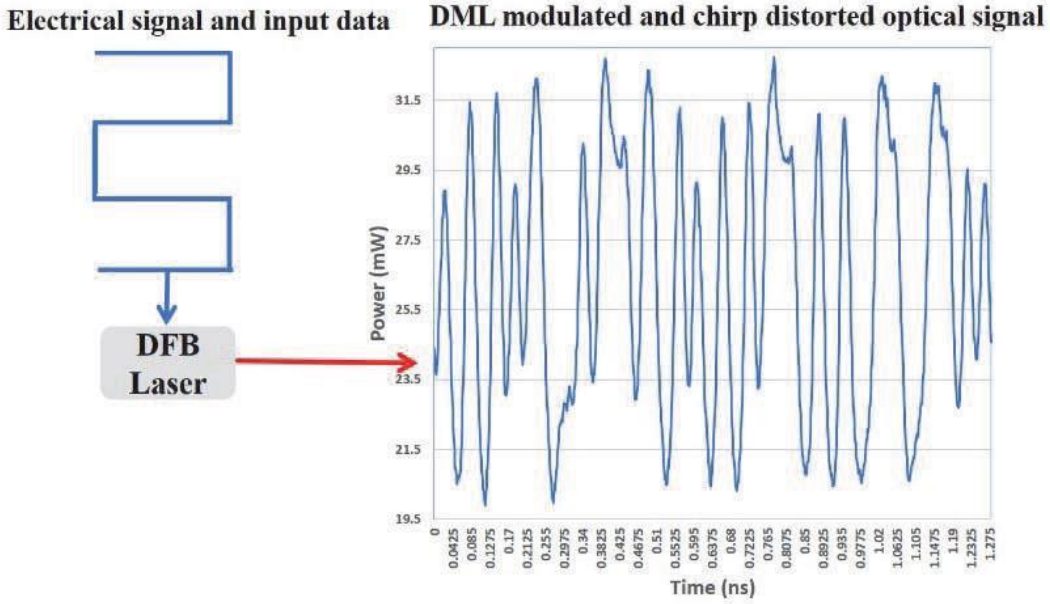


Figure 2.4 Direct NRZ Modulation of a DFB laser via 8

Practically, the most known types of semiconductor lasers such as distributed feedback laser (DFB), constricted-mesa lasers and Fabry-Perot (FP) lasers are the major lasers used for DML purposes. It is important to note that DML is simple and cost-efficient method but can only be applied with low bitrate and short reach as a result of chirp due to spectral broadening associated with the biasing current during modulation. This is due to accompanying phase modulation (PM)

to the desired intensity modulation (IM) during this process. The level of the chirping imposed on the modulated pulse largely depends on the driving condition (Ibias and modulation current (ΔI)) and the laser type.

2.5.1 DML chirping effects

The chirp associated with DML can be subdivided into transient and adiabatic chirp as depicted in figure 2.5.

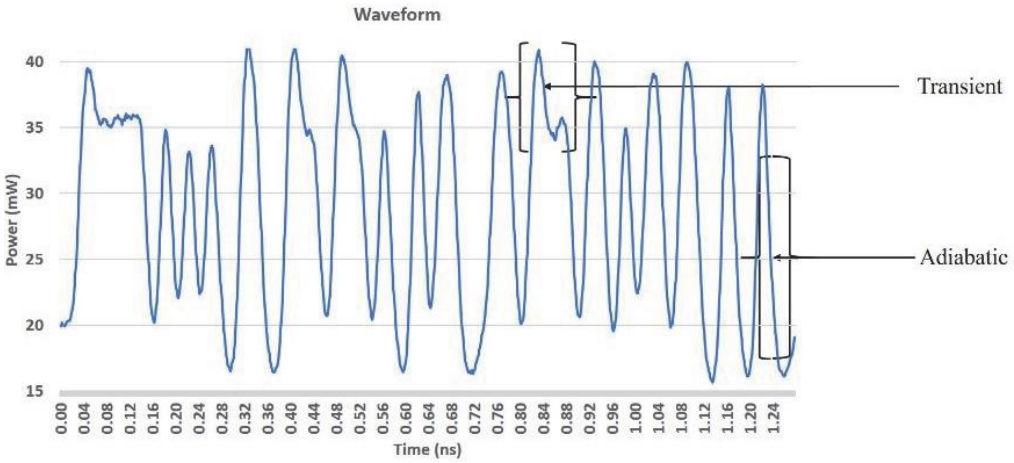


Figure 2.5 Distortion of pulse by transient and adiabatic chirp via 8

The presence of chirp in the modulated pulse leads to high CD and invariably inter-symbol-interference (ISI) which adversely weakens the reach and effects of DML transmission.

As it is shown in figure 2.5, a signal modulated with this technique suffers equally by Transient and Adiabatic chirp. The transient chirp according to [8] is associated with the relatively small frequency difference between the steady state of signal pulse levels of ones and zeros. This frequency difference leads to ringing and significantly obvious overshooting of optical output power and frequency deviations. On the other hand, adiabatic chirp can be described with the damping oscillations and large frequency differences between pulse ones and zeros. To compensate the chirp and the chromatic dispersion various techniques can be used, its own with additional cost and complexity for the transmission line. Some of these approaches that are well known are the use of dispersion compensation fiber (DCF), electrical signal compensations

through decision feedback equalizer (DFE), feedforward equalizer (FFE), continuous-time linear equalizer (CTLE), digital signal processing (DSP), electrical pulse shaping and finally, optical CD compensation. All of whom compensate any fault after the modulation is complete, making the direct modulation techniques less appealing especially for long-haul transmission.

Nevertheless, progressive works to reduce the effect of chirp on DML show improved results. For instance, in a reference of [8], an InGaA1As/InGaA1As multi-quantum well (MQW)-DML was grown on an n-doped InP substrate by shortening the laser cavity length to less than 150 μm via positioning of a passive waveguide in the front of the DFB laser.

CHAPTER 3: PLATFORMS OF EXTRERNAL CONFIGURATIONS AND DIRECTLY CONFIGURED LASER MATERIAL

Optical modulation requires an electro-optic (EO) effect, which provides the necessary change in the optical properties of certain materials when subjected to electric fields of frequency substantially below that of the light wave. When the EO effect modifies the refractive index (the real part of optical permittivity), the modulator is of electro refraction type and this is the case with the Pockels effect, the Kerr electro-optic (or DC Kerr) effect, and free-carrier dispersion (plasma effect). On the other hand, when material losses are modified, the modulator is of electro-absorption type and this is commonly provided by the Franz-Keldysh effect in bulk semiconductors, the quantum confined Stark effect in quantum-well structures, and free carrier absorption. Electro-refraction modulators employ an interferometer (most commonly a Mach-Zehnder structure) or a resonator (such as a microring). Electro-absorption modulators are straight waveguide sections.

3.1 LITHIUM NIOBATE

Lithium Niobate, the most successful and longest in service material, featuring a very strong Pockels effect in structures like LiNbO3, the Lithium Niobate is the material of choice for many years. According to [2] the commonly employed method for defining conventional LN stripe waveguides, mostly in Mach-Zehnder Modulator configurations is the diffusion of titanium into bulk LN wafers. Such waveguides are characterized by low index contrast (0.02or less), translating into weak optical confinement in both horizontal and vertical directions and, thus, limited possibility for high density integration. Spacing between the metal electrodes and the optical waveguides must be large, to keep the losses at reasonable level. Making the use of electrical amplifiers necessary for the driving of a conventional LN-MZM, which with the high driving voltage leads to high energy consumption. This traditional and already in wide use device for

traditional long haul telecom systems doesn't meet the requirements of today, as their described in the introduction. Evolution for LN modulators was made possible with th fabrication of single-crystal LN thin films. This new generation of LN devices are broadly classified in two categories. Theuniform (un-etched) LN thin film and the patterned (etched) LN film. Uniform LN thin films can be oxide-bonded on prefabricated silicon waveguides at room temperatures, meaning they are CMOS compatible in terms of fabrication. The integration of an underlying silicon-photonic circuitry provides the required passive functionality and ensures efficient standardized in/out chip coupling. The device in figure 3.2 is an un-etched LN film having a thickness of 600 nm is bonded on top of a planarized silicon on-insulator (SOI) photonic circuit accommodating a Mach-Zehnder interferometer (MZI), with aluminum electrodes defined over the LN film, with length of 5 mm and Vπ L equal to 6.7 Vcm an ER above 20 dB and EO response above 106GHZ. Hybrid Si- LN waveguides may suffer from reduced light confinement in the LN core and detrimental nonlinearities originating from Si, but different hybrid platforms with lower refractive index, e.g., SiN or tantalum pentoxide, may enable for more light to be confined in LN film and in general better performance of the device.

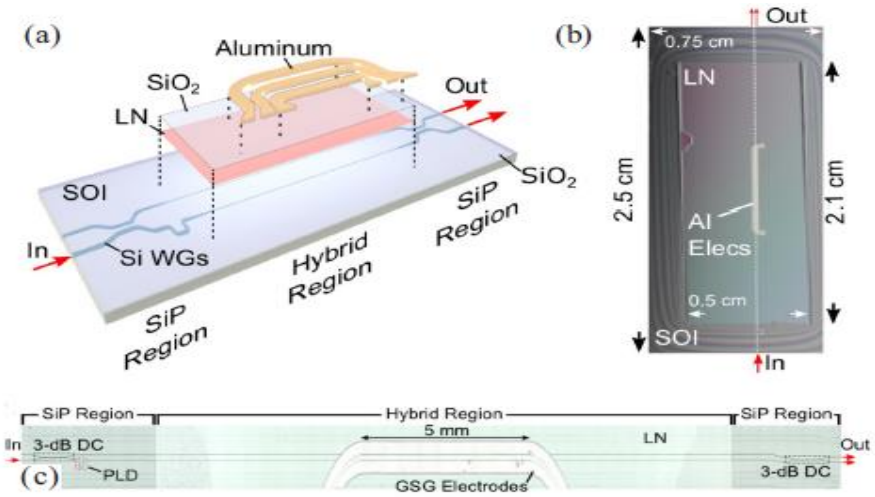


Figure 5.1 Hybrid Si-LN EO Mach-Zehnder modulator. (a) General view showing the un-etched (uniform) LN thin film bonded on top of an MZI written in Si and the aluminum electrodes. The "SiP Regions" accommodate the Si passive circuitry outside the bonded LN film area. (b) SEM image of the hybrid Si-LN modulator. (c) Composite microscope image (not to scale). DC: directional coupler, PLD: path-length difference, GSG: ground-signal-ground, SiP: Si photonics. Adapted with permission from Ref.2 from Ref. 44 2018, The optical society.

The second category of devices includes those with etched single-crystal sub-micron lithium-niobate films. In general Lithium niobate is considered a material hard to etch and in principle produces rough surfaces that suffer from high scattering losses, in the order of 3 dB/cm or higher. Figure 3.2 shows the possibility of ultra-low losses in dry-etched subwavelength LN waveguides with a value as low as ≈0.027 dB/cm An MZI has created by etching a LN thin film of 600 nm thickness for a 20-mm-long device the half-wave voltage Vp of 1.4 V with 30 dB of ER. A modulator of this type allows direct driving by a CMOS circuit. The EO response for a 5-mm device reaches 100 GHz [Fig. 3,2 (c)] and the modulators were also evaluated in various ultra-high data rates including 100 Gbps on-off keying (OOK) and multi-level formats (70 GBd 4-ASK, 70 GBd 8-ASK).

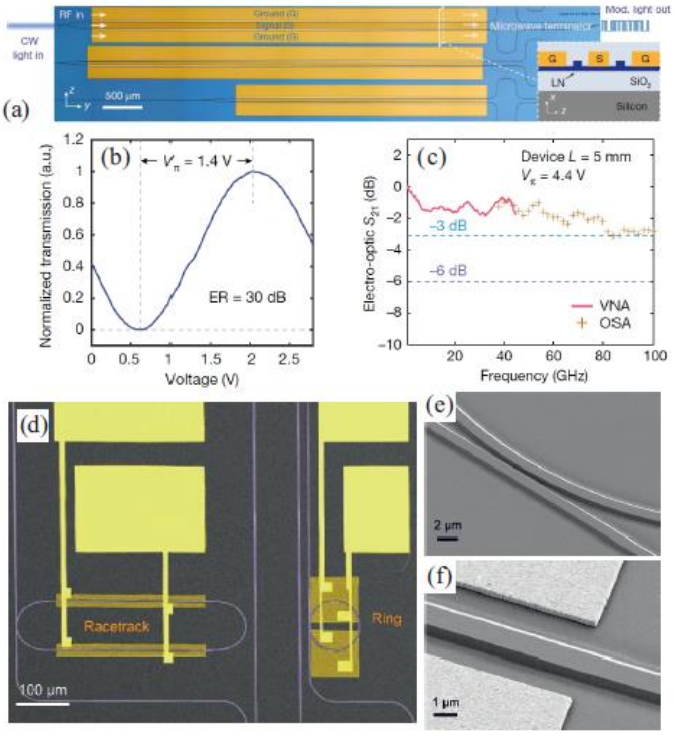


Figure 3.2 Electro-optic devices based on etched single-crystal submicron LN thin films. (a,b,c) Monolithically integrated LN modulators in an MZI configuration. Microscope image showing three MZIs with a cross-section schematic (inset). Normalized optical transmission for a 20-mm device versus applied voltage showing a Vp equal to 1:4 V and an ER of 30 dB. EO response for a 5-mm device showing a 3-dB bandwidth of 100 GHz., Copyright 2018 Springer Nature. (d,e,f) EO racetrack and ring LN modulators. SEM

image of a racetrack and ring modulator, showing also bottom and top electrodes together with the contact pads. Close-up image of the coupling region in the racetrack resonator and close-up view of the metal electrodes with the LN rib waveguide. Adapted with permission from Ref. 2 from Ref. 55. Copyright 2018 The Optical Society.

As a note, it is important to mention that recently have also been experimental demonstration of devices bridging the two categories together. These devices combine a silicon-photonic layer together with an etched LN thin film. Also possible is the Plasmonic EO modulator based on LN substrates, which, according to bibliography [2] describing a plasmonic directional coupler was made by two metal stripes on an un-etched LN substrate, serving both as plasmonic waveguides and signal electrodes.

3.1.1 The effect of LN in relation to the RF circuit

The RF circuitry delivering the modulation signal has a major impact in the performance of LN modulators. The main limitations of the performance is the reduced overlap between electrical and optical modes together with inefficient microwave signal delivery, which can be overcome with the travelling wave electrode (TWEs), typically in the form of a coplanar waveguide in a ground-signal-ground (GSG) configuration. Commonly in use are gold electroplated but also thin deposited aluminum electrodes are used in CMOS compatible devices. For lower the effect of Rf circuit and improving the performance of the LN modulator, as discussed in [2] three main prerequisites should be met (i) minimum mismatch between the optical mode group velocity and the RF wave, (ii) the characteristic impedance of the transmission line should match the source and load impedance (typically 50 W), and (iii) RF losses should also be as low as possible.

3.2 III-V SEMICONDUCTORS

This semiconductor family is between group III (Al, Ga, In) and group V (N,P,As,Sb) of the periodic table. With main representatives been the binary compounds GaAs, InP, GaP, and GaN as well as the ternary InGaAs, InGaP and the quaternary InGaAsP, InGaAlP semiconductors. It

usual for materials to behave in externa stimuli according to one electro optic effect. In this case the EO effect in III-V semiconductors is the resultant of multiple optical processes, including the linear EO effect, the Franz-Keldysh effect in bulk semiconductors or the QCSE in quantum-confined structures, as well as free-carrier effects. The above effects contribute equally to changes in both real and imaginary parts of the optical permittivity, in case of engineering the material, and system parameters can often have a predominant electro-refractive or electro-absorptive nature of the material.The change in the refractive index depends on a signal and the magnetization of the crystal orientation, the RF frequency and the polarization of light. For typical (100) cut and RF field parallel to the surface vector, the linear EO effect becomes maximum for polarization of light parallel to 011, forming only TE-polarized light. The function $|\Delta n| = \frac{1}{2} no^3 r_{41} E$ describes the change in the refractive index, where no is the ordinary refractive index, r41 the EO tensor component, and E the RF field. For GaAs it is about 1.6 r_{41}pm /V, which is noticeably weaker than the EO coefficient of LiNbO3. Compensation for the weaker EO coefficient is achieved with the higher refractive index of III-V semiconductors, while their lower dielectric constant (≈12) also allows for easier phase-matching in ≈traveling-wave designs.

The Franz-Keldysh effect occurs in bulky III-V semiconductors, as changes in the absorbency of nearby band-edge wavelengths under the influence of an electric field due to the widening and sliding of the absorption angles. Operation at the desired wavelength is limited by the maximum permissible field and the value of absorption in the "transparent" stage, which is in fact non-zero even for photon energies below the bandgap, despite the absence of an external electric field, due to the exponential decay of the absorption coefficient.

As stated above in doped III-V semiconductors the free-carrier effect can also contribute to the modulation effect. In [2] the process is described as an accumulation of free carriers increasing the effective bandgap when the conduction and/or valence bands are partially filled (band filling effect), blueshifting the absorption edge. Such changes impact both the real and imaginary part of the complex refractive index.

In terms of fabrication simply rib or ridge waveguides are quite well buried heterogeneous structures with a width of 1.5 to 2 μm and are used for III-V based modulators. Connections and

optical driving are done through an area of high marker of natural semiconductor. The perfect design offers balance between EO-overlap and the high RF-electric field without increasing capacity near band-edge wavelength. MQWs are the most famous configuration with better configurability and better chirp levels.

In chapter 2 EAM are described as simple in-line structures, integrated with DFB's LASER, but coupled to the same chip, to form electro-absorption modulation of lasers (EMLs). EAMs have bandwidth, which exceeds 40 GHz to drive volts of thousands of microns. The predominant representative of the electro-absorption modulator (EAM), typically employing the QCSE in quantum-confined structures to modulate the light intensity at near band-edge wavelengths. The most popular choice is the MQW structure (Fig. 3.3), which exhibits superior modulation properties compared to quantum dots, but also higher chirp values.

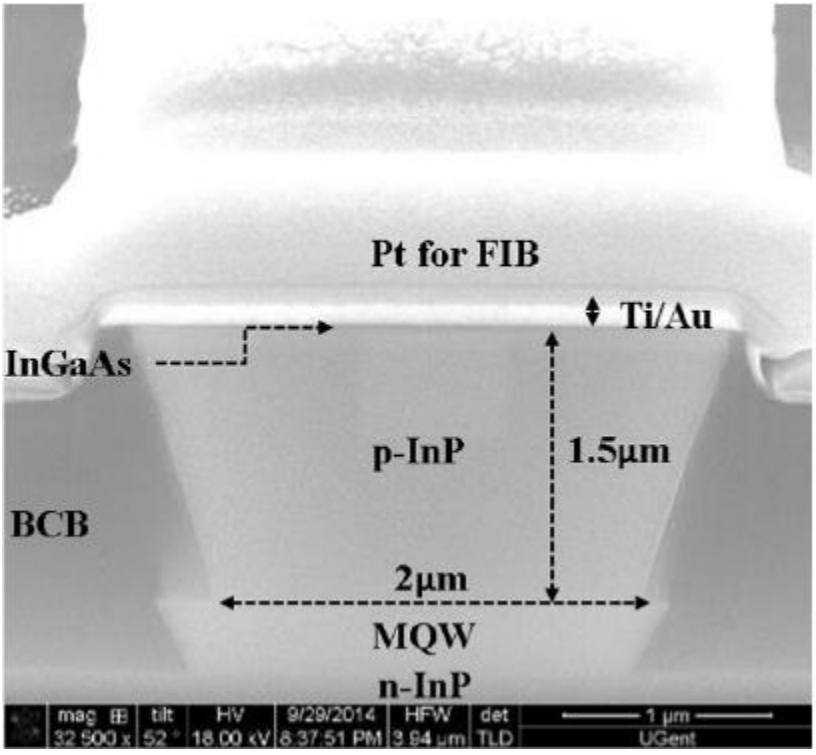


Figure 3.3 SEM picture of the InP-based p-i-n junction in a MQW electro-absorption modulator From Ref. 72. Copyright 2015 The Optical Society.

The short modulation length results in lumped electrode modulators with an RC-limited bandwidth. The latter is in a competing relation with ER, which rises for longer devices at the expense of higher capacitance and increased ILs.The modulation effect (Franz-Keldysh) is enhanced when an InGaAsP waveguide is inserted into an InP platform. In this 100 mm platform we have 56Gbps (NRZ-OOK) and voltage below 1 V. The air bridge structure offers a reduction in capacity and energy consumption reaches 2 fJ/bit. Lumped-electrode EAMs reach up to 100 Gbps with 4-PAM modulation formats, using the technique of flip-chip interface, also with modulation format of PAM 4 a bit of 200 Gbps is reached. Moreover a 300 Gbps bit rate is achieved with DMT configuration and a digital-to-analog converter with a range exceeding 55GHz. However, the length of EAM can be a limiting factor when driven through a 50 Ω system. Towards achieving a better impedance match throughout the bandwidth, again a traveling-wave electro-absorption modulators were suggested. Figure 3.4 depicts a 100 GHz TWEAM with a length of 180 m. The integrated DFB-TWEAM reaches rates of 100-Gbps NRZ-OOK) and 200 Gbps (DMT).

In the case of Mach-Zehnder modulators, a compromise is required between index change and absorption. In order to achieve a short and low-loss phase change drive differentials, soon, lumped electrodes result in the creation of a compact 10-Gbps OOK MZM is achieved with differentially driven, short, lumped electrodes. The MZM is driven with a voltage below 3V and a negative chirp. For higher bit rates travelling-wave electrodes is require. The electrodes are configured either as independent, coplanar microstrips for each interferometric arm or as a series push-pull configuration with a capacitance-loaded coplanar strip line electrode as shown in figure 3.4.

For an InP MZM matching at 50Ω is quite difficult, due to the large capacity of anonymity per length, which is inserted with the p-i-n waveguide structure. A 20-GHz TWE-MZM with 25dB ER allowing 40 Gbps (DQPSK) for 3 Vpp driving voltage and IL=6dB $V\pi L$ = 0.55 Vcm.

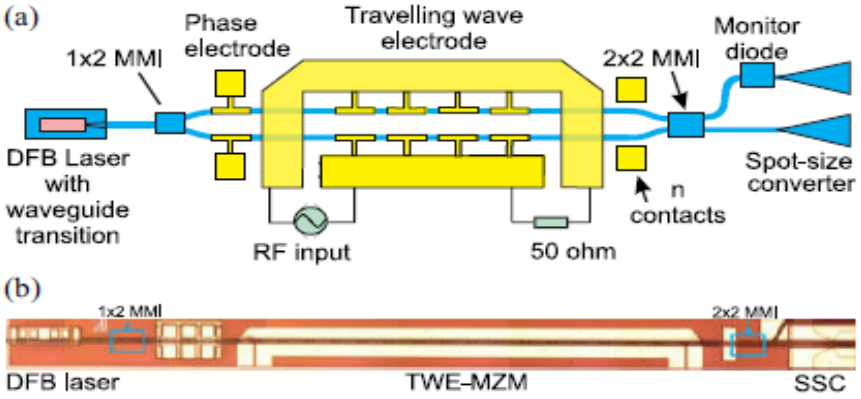


Figure 3.6 (a) Schematic structure of the transmitter, employing a capacitance-loaded traveling-wave-electrode MZM. (b) Photograph of the fabricated DFB-MZM module (0.5*8 mm2). 2016 IEEE.

The series push-pull TWE configuration in Fig. 3.4 exhibits an enhanced bandwidth of 54 GHz, achieving bit rates up to 300 Gbps (PAM) for 0.57 pJ/bit. The use of high-speed SiGe drivers with electronics allows for the existence of a 2-channel (TE and TM) bit rate of 1 Tbps and 32-QAM based on a TWE-MZM structure. The use of n-i-p-n heterostructure instead of conventional p-i-n diode reduces RF-losses. A static 25-dB ER is demonstrated for Vp = 1.5 V and a 4-mm length with an on-chip 8.5-dB IL. Configuration of 128 GBd (QPSK) report rates up to 333Gbps.

In addition to InP MZM, GaAs-based MZMs, employing the GaAs/AlGaAs heterostructure have also been implemented due to their lower cost, superior electrical properties, and temperature stability.

The III-V-based modulators have high efficiency as well as their opportunity to be integrated with optical gain devices (e.g., lasers, amplifiers) and high-speed electronics and the SOI-based platforms are low cost, index contrast, detection efficiency, and CMOS compatibility the increment of the two technologies is very desirable. The solution was provided with a hybrid platform III-V-silicon-photonic, with the fusion of III-V wafer (usually InP) on top of a fully processed SOI wafer using molecular or divinyl siloxane–benzo cyclobutene (DVS- BCB)

3.3 SILICON

Silicon is the most popular material in integrated nanophotonics, mostly due to its almost universal use in electronics, which now offers the advantage of well-known fabrication techniques. Firstly, it is known that because the linear electrooptical effect (Pockels effect) is absent in silicon, the plasma-dispersion effect is used to achieve phase forming with silicon [5]. Using the plasma dispersion effect, various modulation mechanism can be implemented. In any one of them the same principal applies, that is, by changing the free-carriers distribution the silicon waveguide's effective index changes. Regarding the dynamic control of free carries in silicon configuration include capacitor-like structures for carrier accumulation and appropriately biased p-n/p-i-n junctions for carrier depletion/injection. Carrier accumulation schemes employ a thin insulator layer (typically below 10 nm) sandwiched between Si to form a capacitor (silicon-insulator silicon capacitor, SISCAP) so that opposite charge carriers accumulate on each side of the insulator when an external bias is applied, modifying the properties of Si. Generally, highly doped silicon is preferred to lower the series resistance, but it is often the intrinsically high capacitance of SISCAPs that can be the limiting factor regarding EO bandwidth. Despite the potential limitations, high-speed operation with moderate additional (carrier-related) losses are the main characteristics of carrier accumulation configurations, as reported in the literature. On the other hand, carrier depletion (injection) relies on a reverse- (forward-) biased p-n or p-i-n junction to provide carrier inversion (current flow), such junctions are fabricated with standardized and CMOS-compatible processes. Carrier depletion devices are generally characterized by high speed but also high voltage-length.

A more theoretical approach on silicon modulators would assume that the phase shift modulation is proportional to the change of the effective index Δneff as a function of the applied voltage. Using the Drude model for free-carrier absorption [5] the change of refractive index ΔnSi and the loss ΔaSi, as function of free electrons and holes density variations are given by $\Delta nSi(V) = -3.64 \times 10^{-10}\lambda o^2 \Delta n - 3.51 \times 10^{-6}\lambda o^2 \Delta p^{0.8}$ (24) and $\Delta aSi(V) = -3.52 \times 10^{6}\lambda o^2 \Delta n + 2.4 \times 10^{-6}\lambda o^2 \Delta p$ (25)

And so, the change of the effective index as function of the applied voltage is given by

$$\Delta neff = \frac{dneff}{dnSi} \iiint \frac{E \cdot E^* \Delta nSi(V)}{E \times E^*} dxdydz \quad (26)$$

The term dneff=dnSi describes the dependence of the effective index neff on the material index nSi and is very close to one. Here we define x and y to be the vertical and lateral direction, respectively, and z the longitudinal direction of the waveguide.

At the same time the free-carrier absorption is :

$$\Delta \alpha_{pn}(V) = \iiint \frac{E \cdot E^* \Delta aSi(V)}{E \times E^*} dxdydz \quad (27)$$

Whichever topology among those descripted in 2.2 the basic idea is to differentiate the refractive index of silicon waveguide's, changing the dispersion of free carriers. All in all, it is obvious, that increasing the carrier densities and their overlap with the optical field leads to a higher modulation efficiency but also causes higher absorption. The design of a silicon phase shifter is a compromise between efficiency and loss. The carrier transport dynamics (present as RC elements in the circuit level) also needs to be considered as it limits the modulation speed.

Regarding the topology of an MZM in [2] is described the fabrication of 340 *450 nm2 Si-slab waveguide (80-nm slab thickness) to configure 750-mm-long symmetric phase shifters,

placed in both arms of an MZI. A standard practice that increases the overlap between the optical mode and the spatial free-carrier distribution is introducing into the waveguide core a horizontal offset of the p-n junction in this case 50-nm to maximize the modulation efficiency. Applying a higher static reverse-bias to the phase shifters allows for higher electrical bandwidth due to a reduction in the capacitance of the p-n/p-i-n junction (and thus the RC-constant) because of the increase in its space charge region, but also results in higher voltage-length products. Alternatively, forward-biased p-i-n junctions provide lower voltage-length products but require (passive) equalizing RF circuits, which mostly lower the equivalent electrical capacitance to allow for comparably high-speed operation at the expense of modulation efficiency. In [2] is reported a modulator with Vp L = 0.62 Vcm (60mm-long device) with a 17-GHz EO BW and a 2.1-dB dynamic ER at a 25-Gbps transmission rate (OOK).

About the ring topology the reduced device footprint that they offer comes at the expense of optical bandwidth since cavities with high quality factor are characterized by high cavity-photon lifetimes. The authors of [2] refer to two resonators the first having horizontally shifted p-n junction in the guiding area with 7.5-mm-radius, achieving a 14.2 pm/V resonance-frequency shift, translated into a 6.2 dB dynamic ER under 40 Gbps transmission rate (OOK) with 4.8 V peak-to-peak RF signal and moderate static (-2.6 V) reverse bias. The second one is a 2.4-mm-radius disk incorporating a vertical capacitor configuration having an 8 dB dynamic ER at 44 Gbps transmission rate (OOK) with 2.2 Vpp RF signal and only -0.5 V static reverse bias.

3.4 MACH-ZEHNDER SILICON PHOTONIC MODULATON ASSISTED BY PHASE-SHIFTED BRAGG GRATINGS

As it may have been understood there are two general categories of SiP modulators.

MZMs and resonance-based modulators. Because the requirements for the data centers of the future is pushing higher the criteria's for modulators. High performances, such as high modulation bandwidth and low energy-per-bit are prerequisites. MZMs have been extensively studied for high-speed modulation as they offer a wide optical bandwidth and temperature-insensitive operation. In addition, when operated in a push-pull configuration, MZMs enable the generation of chirp-free pulses. Despite these advantages, SiP MZMs are hindered by their low efficiency, resulting in a large footprint and high energy consumption. By enhancing phase modulation, resonators allow a drastic reduction of the phase shifter length. As stated above, micro-ring modulators (MRMs) have a very compact footprint and low power consumption. Combining resonators to a Mach-Zehnder interferometer (MZI) is a promising method to overcome the low modulation efficiency of conventional MZMs. However, he modulation enhancement is obtained at the price of increased temperature sensitivity, similarly, to MRMs. The introduction of cascaded rings in each arm of the MZI was proposed to enlarge the operating temperature range but the free spectral range (FSR) limitation of this design prevents its use in wavelength division multiplexing (WDM) applications. MZMs are loaded with 2D photonic

crystal waveguides (PCWs) to achieve a high modulation efficiency with a large optical bandwidth. Fabrication of 2D-PCW is however well known to be very challenging using standard CMOS manufacturing processes since the design incorporates small features that tend to be smoothed by the optical lithography. Bragg grating devices, which are 1-D PCW, are less sensitive to fabrication errors and are routinely fabricated using UV lithography.

On the other hand is stated in [3], the slow light effect can be obtained by periodic optical structures such as waveguide gratings and photonic crystal under CMOS process, which can optimize the device performance without increasing manufacture complexity. Since the CMOS process is well-known that makes this modulator more appealing for use. The response of the silicon slow light modulator at the bias of 3.5 V is 3 dB EO bandwidth that reaches 110 GHz.

3.5 ELECTRO-OPTIC POLYMERS

A material capable of providing an instantaneous pure phase shift, exactly as in lithium niobate is the Electro-Optic polymers, which molecules are organic chromophores. By a process of deposition [2], the polymer is polarized using a DC bias at fabrication stage alignment of the active chromophores along the direction of the poling electric field is provided. This process is done in elevated temperatures close to their glass-transition temperature Tg After that follows the cooling stage, while still maintain the poling field and so the chromophores keep their orientation. With this process the chromophores gain high molecular hyperpolarizability, which translates into large macroscopic EO activity (r33) in the material. Polymers with r33 exceeding 300 pm/V and they are theoretical predictions of 33 values even above 1000 pm/V. Such EO coefficients exceed those of LN by a factor of 10 or higher. Refractive indices of most polymers in the near infrared are in the 1.5-1.7 range.

Early polymeric electro-optic modulators were based on MZIs made of waveguides with large cross-section (width in the range of a few microns) and low index contrast, with the EO polymer being the waveguide core material. For this class of devices, Vp L values of Vp a few Vcm were routinely reported in experimental demon stations together with static extinction ratios

above 20 dB, thus allowing for sub-1-V operation in devices that were 2-3 cm long. Importantly, the potential for substantial EO bandwidth, well-exceeding 100 GHz, was experiment demonstrated very early. Alternatively, the EO polymer can be introduced as the cladding material in a silicon-core waveguide.

A silicon-organic hybrid Mach-Zehnder modulator is fundamental for improvement of performance of these types of materials. The polymer-clad silicon-slot waveguide that provides phase modulation is a starting point for more efficient devices capable of implement high order of modulation format. Improvements in SOH platform led to IQ modulators that can be directly driven by FPGA outputs at voltages below 0.5 V, thus avoiding digital-to- analog converters or drive amplifiers. Many different modulation formats were successfully tested at different symbol rates, including, with the highest reported rate being 100 GBd 16-QAM (400 Gbps) in Ref [2]. EO-polymer infiltrated photonic-crystal slot waveguides in silicon operating as the phase-shifting elements in MZIs is also an option. This devices, enhanced performance is anticipated due to the slow light effect close to the bandgap edge, with the effective (in-device) r33 acquiring very high values as intensified by the high group index ng. A device like that of 300-mm-long reported in Ref.2 that achieves an average group index ng ≈20 and exhibits a Vp ≈0.97 V (Vp L = 0.29 Vmm) with a measured EO BW of 15 GHz.

Note that a Plasmonic modulators exploiting EO polymers may offer the possibility of further footprint shrinkage.

3.6 TWO-DIMENSIONAL MATERIALS (SILICCON NITRIDE)

Two-dimensional (2D) materials are tunable physical properties under moderate electrical or optical stimuli. Graphene is the best-known representative, but other materials such as silicene, germanene and germanane, black phosphorus (BP), transition metal dichalcogenides (TMDs) (e.g., MoS2,WS2), MXenes (e.g., Ti3CNTx, Ti3C2Tx), and their combinations in Van der Walls heterostructures (e.g., graphene-BP, graphene-TMD, TMD-TMD) have gained a lot of interest lately. Manifesting diverse electronic band structures (from the gapless graphene to the indirect to

direct bandgap transition in TMDs), 2D materials exhibit diverse macroscopic physical properties. Importantly, their high-frequency (optical) electromagnetic properties (real and imaginary part of the complex surface conductivity ss) are tunable under electrical stimulation and as such are considered for electrooptic (both electro-absorption and electro-refraction) modulation. Typically, the tunability is introduced by electrical gating, which modifies the carrier distribution and consequently affects the allowed electron transitions due to the Pauli blocking principle.

An important modulator of this category is the platform of LioNix, they implemented a stress-optic phase modulator, in which the refractive index of the waveguiding materials is controlled by the stress-optic effect induced by actuating a 2 μm thick PZT (lead zirconate titanate) layer on top of the TriPleX waveguide geometry. The efficiency of the modulator is optimized by, amongst others, focusing the applied stress in the waveguide core region through a local increase of the top cladding. This platform is further explained in chapter 4.

3.7 PHASE CHANGE MATERIALS

Materials that are characterized by the phase change effect are those that experience phase transition that can be electrically driven. The most widely investigated modulator of this type is the VO2 in integrated silicon-photonic modulators. Efficient electro-optic modulators can be demonstrated by integrating VO2 inclusions in a waveguide and exploiting the different waveguiding characteristics at the two states of VO2 (insulating and metallic) by engineering the mode overlap with the material. In [2], an EAM with high extinction ratio reaching 12 dB has been experimentally demonstrated by coating a silicon-ridge waveguide with a strip of VO2 which is only 1 mm long along the propagation direction. Several other approaches of PCM modulator have been mentioned in literature, none with experimental verification.

3.8 INGAAIAS-BASED MQWS AND PHC

In addition to external configuration techniques, direct modulated lasers (DMLs) are also commercially available, especially for short-distance optical communications applications. Recent developments in DMLs have highlighted their suitability for low-consumption and high-capacity optical interfaces [2].

Changes in the density of carriers and photons within the visual cavity resulted in interference with wavelength and power, i.e. adiabatic chirp, which obviously underestimated the qualitative characteristics of the transmission and caused changes in the phase for the wave of transmission. As an immediate consequence of the fact that the external modulators are preferred for high-speed transmission on the low-loss wavelength of 1.55 mm. DMLs were limited for transmissions of 10- and 100-Gbps and up to 100 km on the zero-dispersion wavelength.

In general, DMLs have a higher output power compared to bias current and are therefore considered more efficient. In addition, their small footprint makes them ideal for optical interconnections. However, by reducing the transmission distance, it also requires a reduction in their energy operation is also required, i.e., in bias current, at small values comparable to those of their corresponding electrics. Bias current, without the density of the current falling below the lasing threshold, is preferred to reduce the active laser volume. The rate of increase in profit based on the inputs) is beneficial for the more efficient configuration leads to reduction of bias current. Differential gain depends on the material of the substrate, usually it is a quantum-confined III-V semiconductor structures and it can be increased by enhancing the quantum confinement of carriers, the optical confinement, and the optical feedback from the reflector, as well as adjusting the detuning between the lasing wavelength and the gain peak wavelength (it refers to the frequency of the oscillation output power until the laser is stabilized, and its value should be as high as possible). The latter in the case of DMLs of course involves a trade-off between energy consumption and bandwidth. Major factors that determine the damping effect are the nonlinear properties of the gain material, the differential gain, and the photon lifetime. Therefore, despite the very simple idea on which DMLs are based, a laser of immediate configuration of small consumption and wide range is a rather difficult engineering problem.

As DMLs common and well-known structures such as distributed feedback(DFB) and distributed reflector (DR) lasers can be used, so can vertical-cavity surface-emitting lasers(VCSELs). DFB and DR use either ridge waveguide or buried mesa heterostructure have a length of 100 to 200 mm and a modulation rate of 56 Gbps (NRZ-OOK). Usually for the active range are selected InGaAlAs-based MQWs are selected, due to the large displacement of the conductivity band they have, which leads to stronger quantum restriction and operation without cooling requirements, which is energy beneficial. The consumption is in the order of a few pj/bits, however this value should not be compared with the frequently reported fJ/bit value of the external modulators, as they also require a laser source which they must configure, which is usually quite inefficient. Short-wavelength laser (850-1060 nm) multimode VCSELs are based on the GaAs system, which offers the opportunity for dispersed Bragg reflectors of high degree of reflection. They are mainly used in short-distance applications, mainly for coupling optics within datacenter and for supercomputers, and limit the dispersion of mode. VCSELs have a bandwidth of 22 GHz, and reach rates of up to 50 Gbps (NRZOOK) with energy consumption of 130 fJ /bit. Research around InP-based VCSELs seeks to reduce the active area and better coordinate lasing Wavelength. In this direction, that is, reducing the active area of the laser, can be achieved by the photonic crystal platform (PhC), which provides a much higher reflection value than the semiconductor DBRs used in VCSELs. PhC lasers offer high-Q, and very small cavities along with the potential for lateral current injection scheme. In reference [2] the embedded active region PhC (LEAP) laser with dimensions 2.5-mm-long and 0.3-mm-wide active region achieves a transmission rate of 10-Gbps rate with the low consumption of 4.4 fJ/bit. Despite the reduced energy function, lasers with reduced active volume provide low optical output power that are often insufficient for standard detection schemes; Reducing optical losses through the monolithic integration of the laser with photodetectors as well as the minimum optical power in the photodetector could facilitate the requirement for greater optical power. Overall, DMLs exhibit bandwidth values that typically do not exceed 35 GHz, with commonly reported rates up to 56 Gbps (NRZ-OOK).

CHAPTER 4: CONFIGURATIONS STUDIED

4.1 BRAGG FORMATIVE

To take advantage of industrial compatibility with CMOS technology, silicon configurators are always limited by esthetically small low EO bandwidth (<67 GHz which prevents the further development of the data link at an overall rate above Tbps. So far, the various types of configurators have been presented, however the design dilemma in the resonant or non-option has not been highlighted, conventional Mach-Zehnder modulators (MZMs) are blocked by high levels of consumption and a large footprint in space, the modulation arms have a fairly millimeter length, due to the low performance of the depletion mode shifter modulators. ring modulators (MRMs) have a more compact footprint in space; however, they have a narrower optical bandwidth and are more sensitive to their operating temperatures, which requires extra energy to control the temperature in real scenarios.

In [7] an ultra-compact silicon slow light modulator compatible with CMOS technology is presented. This configuration has length of 124 μm and the very high EO bandwidth of 110 GHz, which is the highest of the silicon photonic platform, an order of magnitude greater than silicon MRMs. The transmission of OOK signal data over 110 Gbps without digital signal process (DSP) is presented with great success.

4.1.1 Design

The silicon slow light modulator has a configuration length of only 124 mm and adopts the dual-drive design with radiofrequency (RF) GSGSG pads based on the Mach–Zehnder interferometer, as in Figure 4.1(a). It becomes unsurprising that the compact modulator is much smaller than conventional MZMs and hybrid silicon-based LN modulators. In the configuration area, the waveguides consist of Bragg gratings, such as those described theoretically in chapter 2 with a period of 300 nm. Each Bragg resonant unit consists of a Phase shifter with 20 waveguide gratings

on each deck, 10 units are manufactured in each modulation arms. The specific structure, of slow light waveguide is shown in figure 4.1(b), and the intersection of PN junction at different positions is shown in figure 4.1(c). Silicon optoelectronic integration is the main limiting factor in size in the current factor.

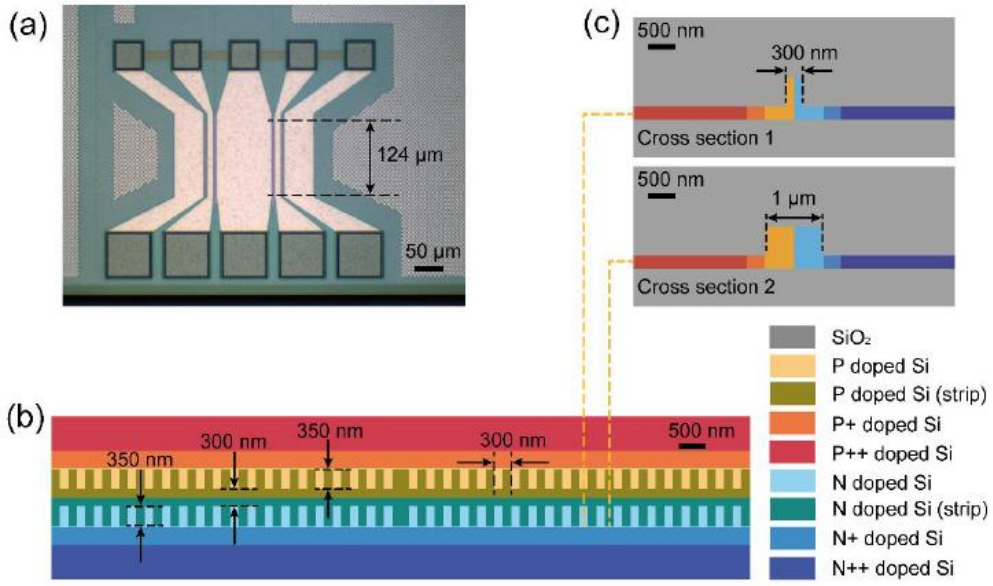


Figure 4.1 «Ultra-compact silicon modulator with 110 GHz bandwidth,» Optica Publishing Group, 2022.

4.1.2 Optical and EO bandwidth

In real operating conditions, the existence of a large optical bandwidth is significant for optical modulation, because thanks to this, a wider operating wavelength and better thermal stability are achieved, which is particularly important for practical applications. In addition, input losses were measured at 6.8 dB, including 1 dB from the two 3 dB couplers, 0.4 dB from waveguide routing and 5.4 dB from modulation shifter. The loss is the same as the standard silicon MZMs with a standard PN junction structure.

In addition, the existence of high EO bandwidth of this configurator is the guarantee of high-speed transmission. Figure 4.2b shows the measured EO of the silicon slow light modulator for bias voltage 3.5 V. The 3 dB EO reaches 110 GHz bandwidth and of all silicon modulators, this one is with the largest EO bandwidth.

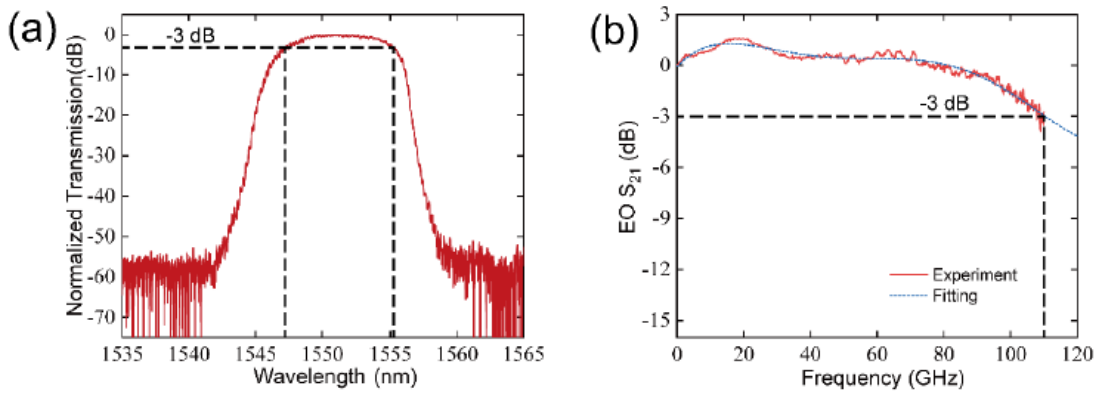


Figure 4.2 a) The transmission spectrum of the silicon slow light modulator. (b) The EO S21 response of the silicon slow light modulator.

4.1.3 Information Transmission Capabilities

The transmission experiment is illustrated in Fig. 13(a). The optical signal of 1550 nm is generated and passing a polarization controller to minimize the coupling loss, the optical signal is sent into the Bragg grating silicon modulator. Here, the OOK signal is generated and amplified by driver and combined with bias voltage to load onto the modulator by RF probe. Then the optical signal generated by the modulator is amplified by an EDFA and gets into the digital serial analyzer (DSA). Due to the record high EO bandwidth of the modulator, the OOK eye diagrams of 100 Gbps and 112 Gbps can be illustrated clearly with extinction ratio (ER) of 3.15 dB and 2.15 dB respectively figure 4.3b.

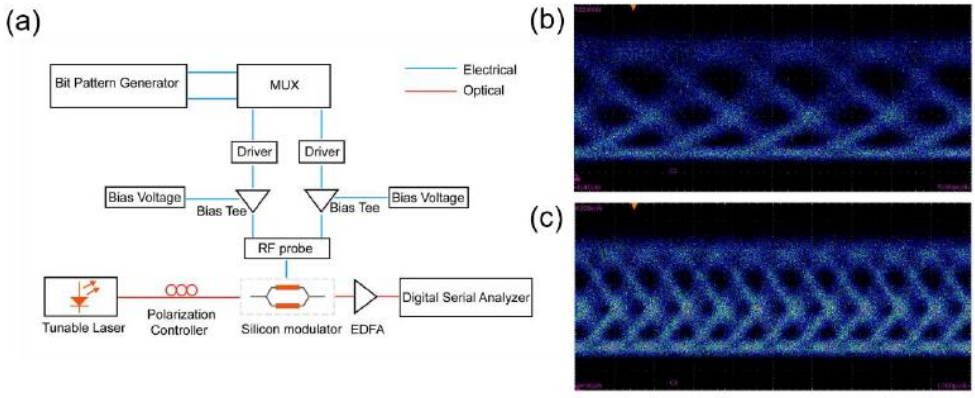


Figure 4.3 Transmission Schematic and b) Optical eye diagram at 100 Gbps with ER of 3.15 dB. The time scale is 5 ps/div. (c) Optical eye diagram at 112 Gbps with ER of 2.15 dB. The time scale is 10 ps/div.

4.2 MODYLATORS SILICON NITRIDE

Silicon Nitride is a dielectric, and therefore in these materials neither Pockels nor carrier-plasma dispersion effect appears, on which the configurators LiNbO3 and Si are based on lead zirconate titanate (PZT) or LiNbO3. In both cases more than 30GHz electro-optical bandwidth is achieved.

In these devices the general idea is to drive the SiN through hybrid waveguides or other types of waveguides which can make configuration based on different mechanisms. The transition from Si- layer to SiN layer has transition loss of less than 0.1dB ensuring that this design can provide a low insertion loss of Si modulators on SiN platforms. An MZM or micro ring modulator can now be inserted into SiN photonic circuits.

Due to the absence of carrier-based plasma dispersion effect and electro-optic, silicon-nitride modulators usually rely on slow and inefficient frequency tuning for simplicity. Like any other integrated photonic platform, so the thermo opotic phase-shifter SiN, work at microseconds speeds or even slower. The thermal resonance of SiN and SiO2, lead to about ten times the electrical power consumption for the same number of index tuning compared to silicon. On the one hand, low-loss-SiN waveguides is likely to lead to large all-round PIC systems. On the other hand, various thermal disputes (crosstalk) impose restrictions. To achieve a low-loss and low-energy resonance method, significant progress in piezoelectric resonance of photonic devices and SiN circuits has been made. They consume a negligible amount of static power, but so much so that it enables them to keep a phase state stable. Piezoelectric resonance has been used for optical modulation, and Mach Zehnder (MZI) construction. The studied type of this device is the one designed by the team of LioniX[11]. They fabricated a stress-optic modulator using a standard double stripe TriPleX™ geometry. To evaluate the dependence of the stress-optic effect with the top cladding thicknesses, tc, they deposited top claddings with a thickness of 2 μm and 3 μm on two wafers. Afterwards a bottom electrode consisting of a 10 nm thick Ti adhesive layer and a 100 nm thick Pt layer was deposited. The PZT layer with tPZT = 2 μm was grown on top of this electrode using Solmates SMP-700 pulsed laser deposition (PLD) equipment. PZT deposited by PLD allows for the growth of high-quality layers which has recently become available for large wafer sizes and at commercial throughput. To ensure the quality of the deposited PZT layer, we

measured the transverse piezoelectric coefficient, e31, of -18 to -20 C/m2, using simultaneously produced test structures from the same wafer. Finally, a Pt top electrode with a thickness of 100 nm was deposited with various widths, w, and lengths, l. A scanning electrode microscope (SEM) picture of the LioniX platform

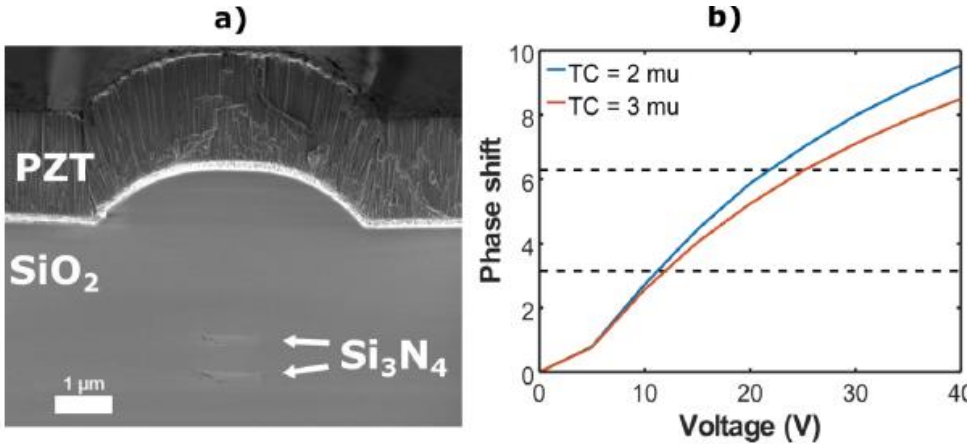


Figure 4.4 a) SEM picture of the LioniX platform b) Phase shift versus driving voltage

The measured a half-wave voltage, Vπ, (i.e. a phase shift of π) at 12 V and 11 V for tC = 3 μm and 2 μm, respectively figure 4.4. A phase shift of 2π was measured V = 25 V and 22 V for tc = 3 μm and 2 μm, respectively. The response of the stress-optic actuator has a proportional regime between 5 and 15 V, for higher voltages the slope of the curve decreases with increasing voltages. The reason for the decrease in modulation strength is the decrease of the transverse piezoelectric coefficient of the PZT layer after it reached its maximum at electric field strengths of around 10 V/μm. This decrease matches with the measured hysteresis-curve of PZT test structures that were fabricated on the same wafer.

4.3 SILICON MZM

As the main representative of this technology, the modulator that was chosen, is the one described in [6]. It is a high-speed silicon modulator, of Mach Zehnder interferometer (MZI) architecture with reversed biased pn diode integrated into each arm, as shown in figure 4.5.

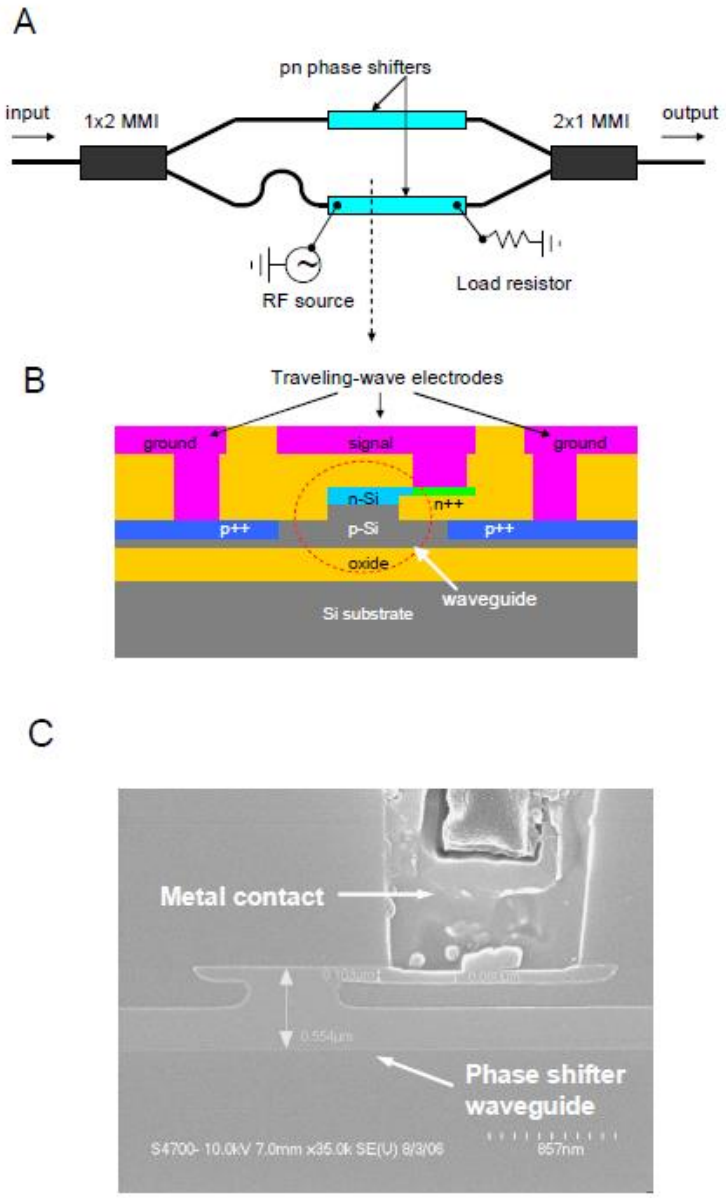


Figure 4.5 (A) Top view of an asymmetric Mach-Zehnder interferometer silicon modulator

containing two pn junction based phase shifters. The waveguide splitter is an 1x2 multi-mode interference (MMI) coupler. The RF signal is coupled to the travelling wave electrode from the optical input side and termination load is added to the output side. (B) Cross-sectional view of a pn junction waveguide phase shifter in Silicon-On-Insulator. The coplanar waveguide electrode has a signal metal width of ~6 μm and a signal-ground metal separation of ~3 μm. The metal thickness is ~1.5 μm. The high-frequency characteristic impedance of the travelling wave electrode is ~20 Ω. (C) Scanning electron microscope (SEM) image of a pn diode phase shifter waveguide.

An additional 1x2 multi-mode interference (MMI) coupler is also used, which is preferred over a directional coupler, for the sake of the longer operating range depending on the wavelength and the highest strength fabrication. The MZI with the identical armrests has wide bandwidth and works for a wavelength from 1.33 to 1.55 m. The main active element of a silicon modulator is the reverse biased pn junction phase shifter. Each phase shifter, consists of a p-type doped crystalline silicon rib waveguide, which has a width of ~0.6 μm and a rib and a height of ~0.5 m, while the top layer n -type doped silicon has a width of ~1.8 mm. This thin layer of about 1 mm is formed using a non-selective epitaxial silicon growth process andi s prefer for pn junction formation and electrical contacts. The p-doping concentration is ~ 1.5x1017 cm-3, while the n-doping concentration varies from ~3x1018 cm-3 up to ~1.5x1017 cm-3, for the last layer of pn junction. To ensure good ohmic contact between the silicon and the metal contacts, two plates of ~1mm, which are located away enough (~0.3μm m) on both sides of both rib edge and thin cap layer, are strongly doped with a donor concentration of ~1x1020 cm^{-3}. The process is designed to target pn junction at about 0.4 μm above the buried oxide to allow for optimal tropical coating with the depletion area. Since the n-doping concentration is much higher than the p-doping concentration, carrier depletion under reversed biased occurs mainly in the p-type region. To reduce the RC limitations of the reaction frequency of the modulator, a travelling wave electrode is added based on the coplanar waveguide structure image 14. Single-sided asymmetrical design of the top layer of silicon is used to reduce the capacity of the phase shifter. The metal layer "signal" has a width of ~6 μm and is connected to the silicon area of type n through a contact of 1 μm. The separation between the layers of signal and grounded metal is ~3μm and the thickness of the metal is ~1.5 μm. The RF travelling wave coplanar waveguide and the modulator optical waveguide are

designed in such a way that both the electrical and optical signals co-propagate along the phase shifter at similar speeds, while at the same time the RF attenuation is kept at low levels. For asymmetrically doped pn (the n-doping concentration is much higher than the p-doping concentration), the exhaustion amplitude (WD) can be approached with

$$W_D = \left(\frac{2\varepsilon_0\varepsilon_r(V_{Bi}+V_{app})}{eN_A}\right)^{1/2} (28)$$

Where e_0 is he vacuum permeability and $e_r$the relative low frequency permeability of silicon, e is the electron charge, NA is the receiver concentration, VBi is the built-in voltage, and Vapp is the applied voltage. Changing the depletion width of a pn junction is equivalent to a change in the free carrier density, thus changing the bias voltage, one can achieve regulation of the refractive index through the free carrier plasma dispersion effect.

In the experimental analysis of [6] the output intensity of the MZI depends on both the wavelength and the phase modulation induced by the bias voltage.

Completing this chapter, all the latest ultra-Fast modulators, that have been studied can be seen in the next table

Platform and Section	VπL(Vcm)	ER(dB)	EO bandwidth(GHz)
Hybrid LN-SI(3.1)	6.7	20	106
LN-thin film(3.1)	0.7	30	100
InP MZM (3.2)	0.55	25	55
Silicon MZM(3.3)	0.62	2.1	17
Silicon MRM(3.3)	-	8	-
Silicon Bragg(4.1)	-	3	110
Polymer(3.5)	2.9	20	15
LioniX(4.2)	0.06	0.1	30

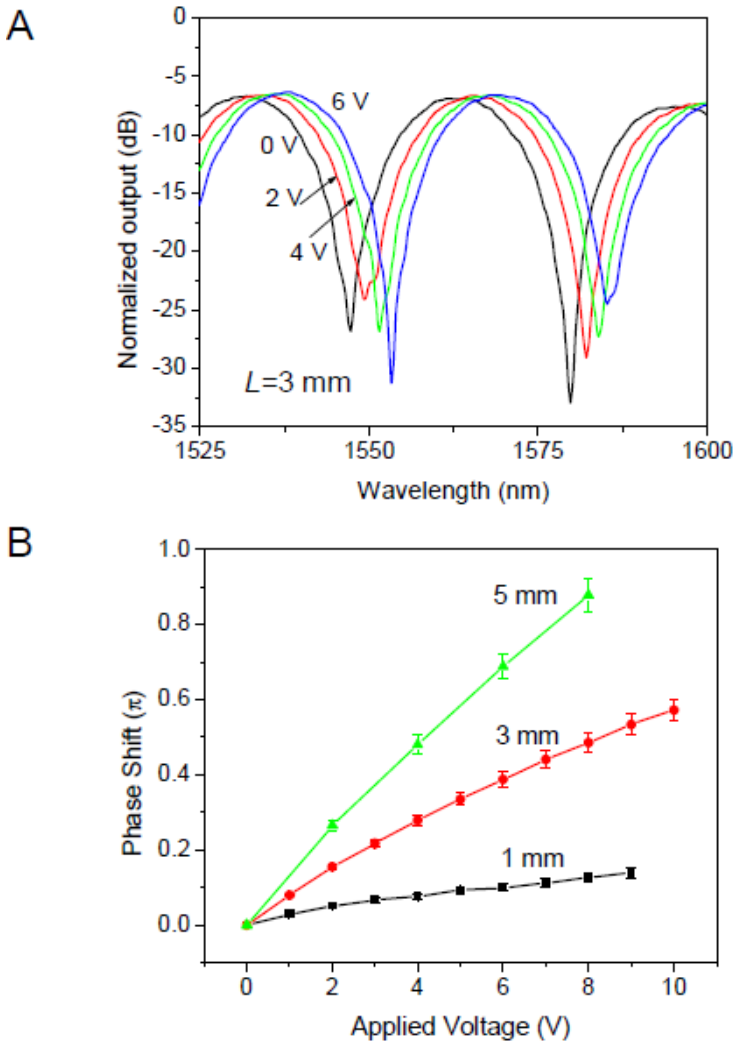


Figure 4.6 The output spectra of a MZI modulator having 3 mm long phase shifters for various voltages applied to one of the arms. The MZI output is normalized to the output of a straight waveguide with the same waveguide length without pn junction and drive voltage. (B) The phase shift of an individual phase shifter vs. the drive voltage for the wavelength round 1550 nm for different phase shifter lengths.

The bias-induced increase in the effective refractive index of the phase Shifter leads to a shift with increasing applied voltage at the MZI output spectrum It can also be seen from Fig. (a) that the DC extinction ratio of the MZI modulator is greater than 20 dB over a wide wavelength range. The on-chip insertion loss is ~7 dB when the MZI is in the "on" state, which is defined here as the maximum optical output intensity of the MZI. This on-chip insertion loss (excluding coupling loss)

includes ~1 dB passive waveguide transmission loss, ~0.5 dB MMI coupler loss, and ~5.4 dB phase shifter loss, which can be attributed primarily to the dopants.

4.4 HYBRID MODEL

This section refers mostly to a type of modulation rather than a specific modulator and that because it is dedicated to a hybrid modulations format between a direct modulated laser and an electro-absorption modulator as the one described in [8].It is known that different limitation can be addressed both to DML and EML schemes, but at the same time both are well known, widely in use and affordable schemes and optimization is worth a try. In [8] focus is driven upon the fact that DML can only be used for relatively lower speed 25 Gb/s and cannot be transmitted beyond 10 km for data-center interconnect (DCI) and passive optical networks (PON) systems and external modulation through EAM is limited by high IL values to address requirements of high ER. As a result a combination of these technologies that will minimize their negative behavior and enhance their pros is suggested. So, the modulated optical signal from DML is launched into the optical signal input of the EAM to re-modulate the optical signal for intensity signal generation. Both components have previously optimized, in the case of the laser, that is shown in the following matrix:

BitRate	10 Gb/s
Wavelength	1.57 μm
Laser Bias Current	90 mA
Laser Confinement Factor	0.5
Henry Linewidth Enhancement Factor	3.0

Table 7 Optimized parameters of the DML.

In the case of the EAM the length of 5μm is the length that offers the best error rate as that is the reason that is chosen.

CHAPTER 5: OPTICAL DIGITAL TO ANALOG CONVERTER VPI-PHOTONICS

This chapter is dedicated to the integration of specific platforms of preference in one of the key elements of any transmission system, that of the Optical Digital to analog converter. Electronic Digital to Analog Converters (eDACs), are key interfaces from the digital to the analog domain. In high-speed digital optical transmitters, the Digital to Optical (D/O) translation typically comprises power consuming and costly eDAC-based data conversion, followed by analogue optical modulation. As described in chapter 2 the conventional method is using eDACs to drive multilevel analog signals to the optical modulator. However, in subsection 2.1.5 the topology of segmented MZM is presented, which ,as stated, enables the conversion of higher modulation formats with simpler eDACs, which is advantageous, from the viewpoints of performance, energy efficiency, complexity, and cost reduction. To adopt direct Digital to Optical domain (D/O), conversion, a perfect segmented MZM(SEMZM) must implemented, to eliminate the eDAC intermediaries as the one descripted in [9]. This would be particularly useful in future generations along the roadmap of ultra-high-speed photonic interconnects, as eDAC technology is ever more expensive and is becoming increasingly difficult to keep scaling up in data rate, while keeping power dissipation in check and retaining ENOB performance. An oDAC is essentially an optical multilevel constellation generator (e.g., a source of optical PAM4 or PAM8 in one-dimension (1D). The novel design oDAC, that is the subject of this Thesis, is driven right from the digital input bitstream, without internally resorting to intermediary electrical multilevel signals, thus, eliminating the problematic ultra-high speed eDACs. As comparison a simple MZM driven by a multilevel eDAC is implement in the first section of this chapter. Multiple analog two level electrical signals, as generated by an array of 1-bit electrical drivers (each driven by a bit of the input codeword) are an integral part of oDAC constitution, as each of these analog two-level signals drives an elementary 1-bit modulation-gate. The optical outputs of the array of 1-bit gates are superposed in a suitable optical field characteristic (phase or amplitude), akin to addition of currents or voltages from elementary electrical sources in an eDAC. In oDACs, the analog summation of elementary sources occurs in the optical domain.

Silicon has been chosen as the platform of choice for all the following oDACs designed (its advantages over other can be seen in chapter 3 section 3.3.) To objectively evaluate the performance of the two MZM structures similar phase shifters in terms of material and the same electrode design for the two modulators is used. Both simulations achieve optical PAM4. In case of the hybrid model an ePAM2 to optical PAM4 is presented to verify the good operation of the device.

At the end of the chapter a novel design of a parallel multi-level oDAC with segmented MZM at its arm is presented. This architecture has never been presented before and the idea came from combining the serial oDAC with the parallel one, as these was descripted in [10].

5.1 IMPLEMENTATION OF A SIMPLE MZM

The MZM that is implemented is equivalent to the physical silicon modulator described in section 4.3. The silicon modulator is designed and driven in series-push pull (SPP)scheme, where a positive phase shift in one arm is accompanied by a negative phase shift of equal strength in the other arm. One advantage of the SPP MZM is that it requires one RF signal to drive the modulator. This noticeably lowers the system complexity, when operating the MZM for PAM-4 modulations, since addition of any RF signal requires further microwave analysis and can trigger unwanted cross talk between channels. Figure 5.1 shows the MZM implementation in the VPI Photonics simulation tool. From left to right the schematic has one optical input, which is coupled with an ideal coupler of ratio equal to one half and then the outputs of the first coupler are connected to the phase shifter. These phase shifters were designed as a part of this Thesis and among other parameters, that will be discussed, they have a parameter of sign. So the upper one is assigned with sign equal to1 and the other one is assigned to be negative. Both are driven by electrical signals and their outputs are inserted to the respective input of the second coupler. Because the couplers add an unwanted phase difference of 90 degrees each, a PM module with constant value of -180 is used to cancel that.

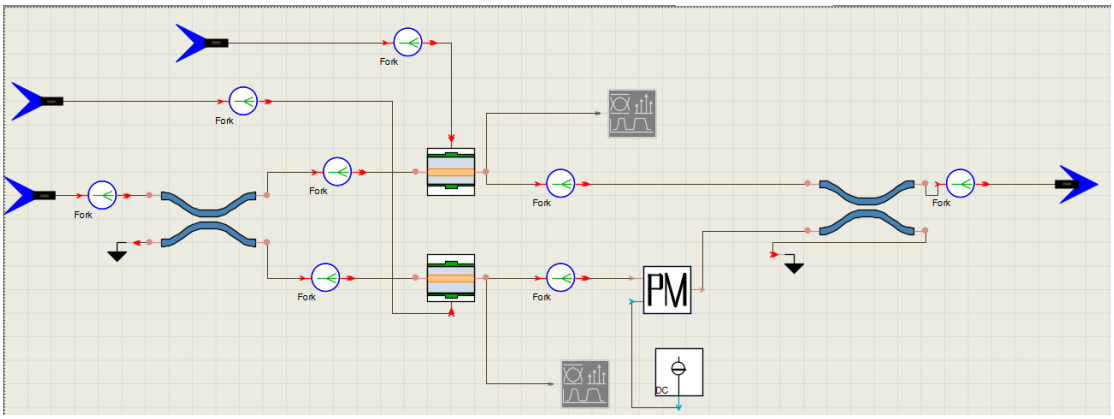


Figure 7.1 Implementation of MZM in Vpi photonics.

Now the main intrest is on the characterization of the phase shifter. A phase shifter with a silicon waveguide and a travelling wave electrode is implemented Φigure 5.2 . As stated in [10] the phase difference of the phase-shifter is described a function of V and L. This can also be seen in the experimental data of figure 4.6b.

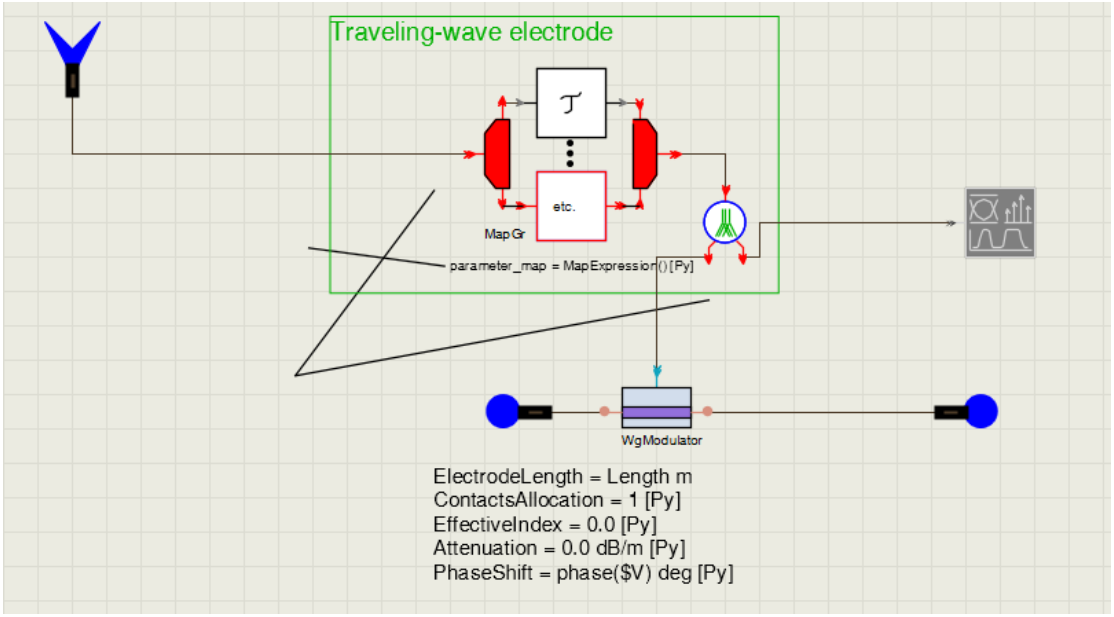


Figure 5.2 Inside the phase shifter of the MZM of figure 5.2.

More specifically , for a generic MZM or for a push-pull dual phase-modulator (PM), of length L, driven at voltage V, the induced phase shift is given by the following:

$$\varphi = \frac{V \cdot L}{V_\pi \cdot L_\pi} \qquad (29)$$

where $L\pi$ is the particular "reference" electrode length that Vπ is stated at ($V\pi$ defined as the voltage needed to inducepi-phaseshift in a waveguide with electrodes length $L\pi$). So a python script is written and the phase parameters of the waveguide change accordingly to phase

$$(V) = (-1) * (sgn) * (90) * \left(\frac{L}{Lp}\right) * \left(\frac{V}{Vp}\right) + sgn * 90 \qquad (30)$$

For the minus and plus 90 degrees explanations will be given. Taking under consideration the technology chapter 4 section 4.3 the $L\pi$ is equal to 3mm and $V\pi$ to 10 volts.

The phase shifter schematic, that is presented in figure 5.2 takes as physical parameters the Length, the GroupIndex, NumberOfDeviceSections, DelayTime and as previously mentioned the sign. The transfer function TF of the MZM in the optical domain is described as

$$Fc = sin[b[c]\Delta\varphi] \quad (31)$$

The index labeling the OCs levels/codewords, ranging over {1,2,3,4} for a PAM4 OC. For PAM4, the oDAC 'code'

$$b \equiv \left[b1[c], b0[c] \right]_{,c=1,2,3,4} \quad (32)$$

the set of four two-bit codewords, corresponding to the four PAM4 levels respectively given for a DD OC by

$$b \equiv \{\{0,0],[0,1],[1,0],[1,1]\} \quad (33)$$

The goal is creating the Transfer Function Fc, that is achieved by choosing the couplers and implementig the MZM architecture. Knowing that its phase shifter has transfer function equal to the

$$A_{out}(t) = e^{j\Delta\varphi 1} A_{in(t-\tau g)} \quad (34)$$

and the fact that the input amplitude is divided by 2 due to the coupler's ratio factor, that moves everything closer to the creation of sine fuction. The reason being that the Euler's equation $\frac{e^{j\theta}+e^{-j\theta}}{2} = cos\theta$ creates the cosine and $\frac{e^{j\theta}-e^{-j\theta}}{2j} = sin\theta$ the sine.

Paying attention to the fact that the coupler add the two signals of each path creating in this way the cosine fuction, and there is not such a thing as negative coupling ratio, only the cosine can be generated. The goal of creating the sine fuction is achieved using the trigonemtric equation

$$sin\theta = cos(90 - \theta) \quad (35)$$

In terms of vpi simulation that is achieved by changing the Δφ equation to the form of

$$\Delta\varphi' = 90 - \Delta\varphi \quad (36)$$

In the python scripted this is writed as:

$$phase(V) = -1 * (sgn) * (90) * (L/Lp) * (V/Vp) + sgn * 90 \quad (37)$$

Now that the MZM is implemented, a PAM4 electrical driver, figure 5.3 uper left side, using two PRBS generators and a driver is used to generate an ePAM4 signal figure 5.3 , plus a module that transforms the generated elctrical blocks to saples for the waveguides, which are nested inside the MZM, that is send to the modulator. A DFB laser that produce a continuous wave optical signal is send to the optical input of the modulator.

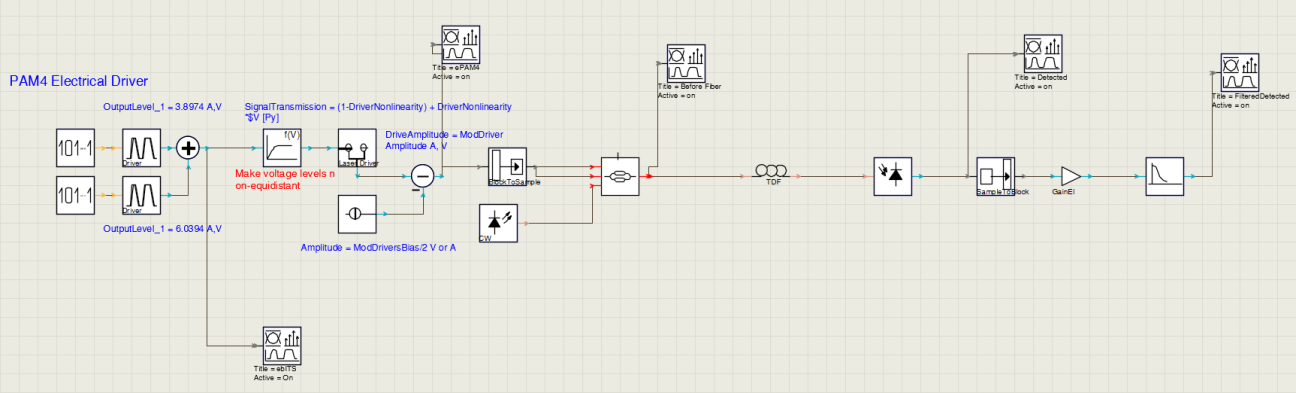


Figure 5.3 Transmission schematic, ePAM4 driving the MZM of figure 5.1

Then the oPAM4 that is created is send through an ideal optical fiber to the photodetector and then through a amplifier and a Bessel's low-pass filter the eye diagram of figure 5.2 is received.

The fact that between levels of the optical PAM 4 signal exists equal spacing figure 5.5, leads to the conclusion that everything work in order and the optical PAM 4 signal is perfect.

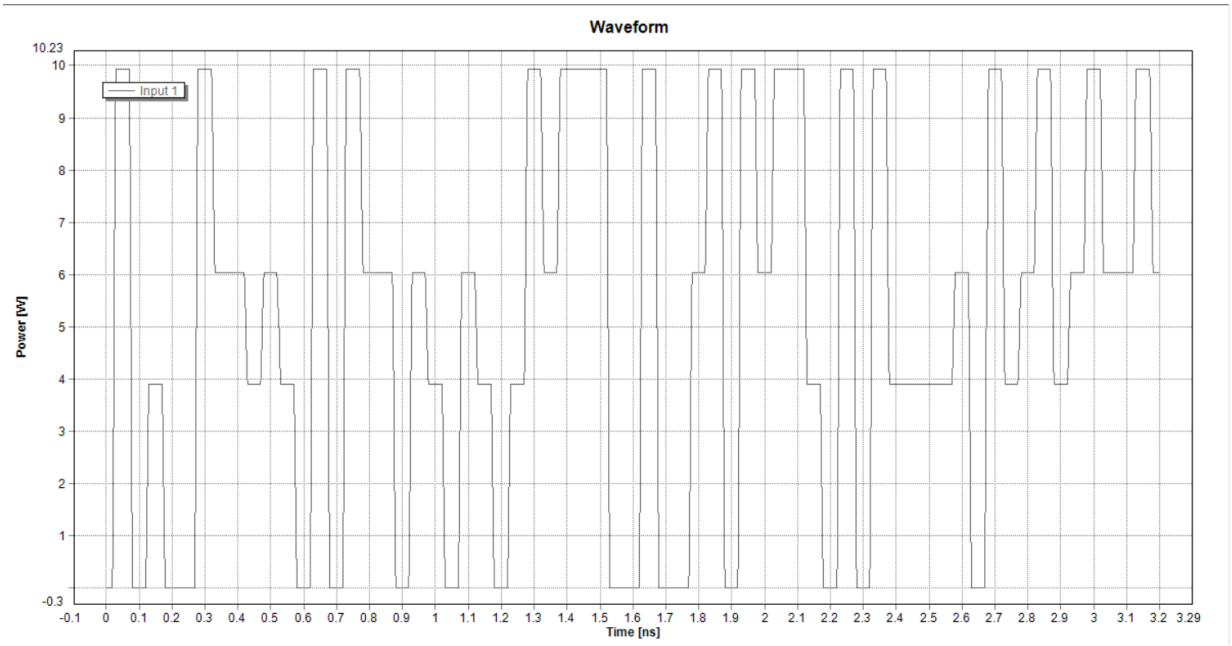


Figure 5.4 oPAM4 received after the fiber in the simulation of MZM.

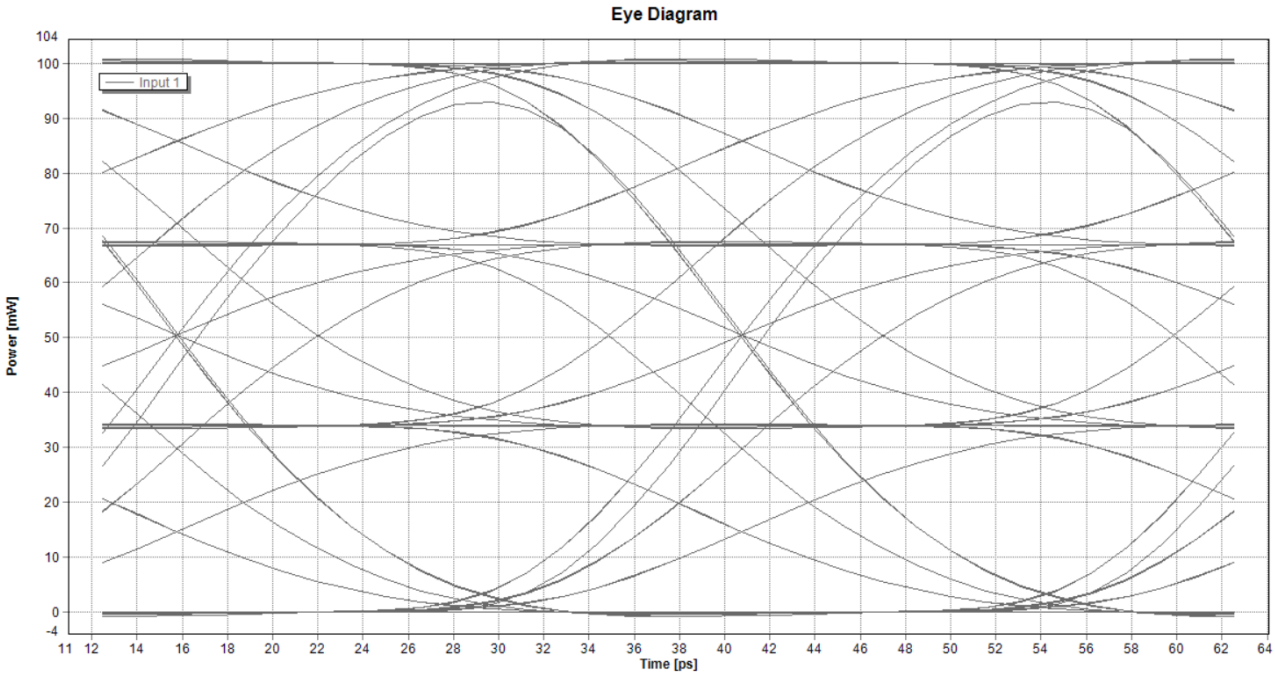


Figure 5.5 Eye Diagram of the optical pulse of figure 5.4.

5.2 IMPLEMENTATION OF HYBRID SML-EAM MODULE

Another modulation technique that of hybrid modulation, as the one described in chapter 4 is also implemented in VPI photonics. The advantage of this technique is the fact that it is a combination of already well known and commercially available components. In section for 4.4 it is described how this technique combines the DML and EAM in a manner that the faults of the separate techniques are minimized, and the overall performance is improved. The implementation in VPI of the hybrid modulator is not complete, due to lack of information about the transfer function of the EAM, in which [8] was based. So, an EAM with physical parameters of length equal to 650 μm, MQW active region and MQW differential index equal -1e-29 is used. The DML laser has a length of 600 μm, Laser Confinement Factor 0.5, Henry Linewidth Enhancement Factor 3.0 and is driven with 90 mA. The simulation schematic contains the same electric PAM 4 signal generator with the MZM simulation. The generated signal is sent to two different drivers, one is driving the DFB laser and the other one the EAM figure 5.6. Figure 5.7 shows the generated optical PAM4, which shows better performance of the directly modulated NRZ system of the figure 5.8.

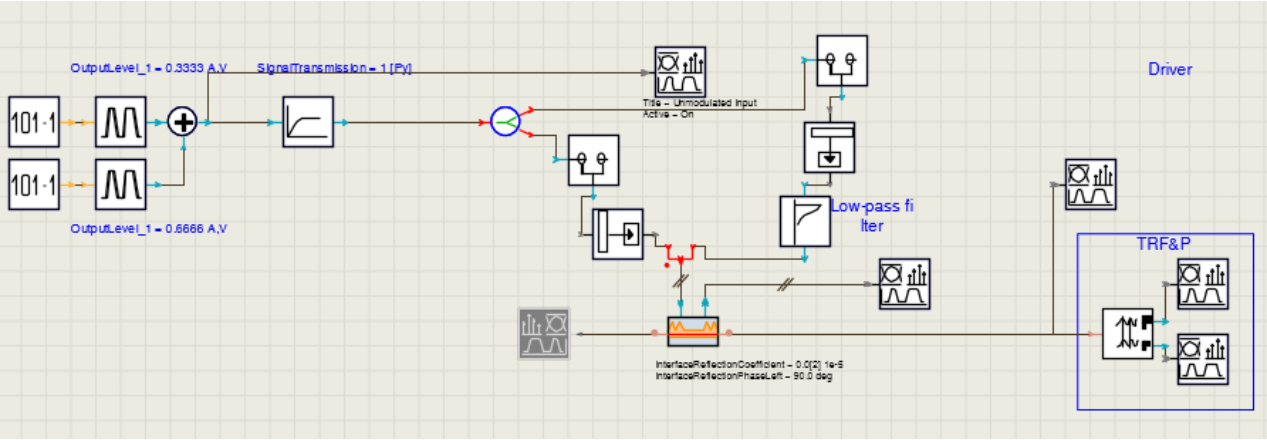


Figure 5.6 Transmission Simulation of Hybrid DML-EAM signal.

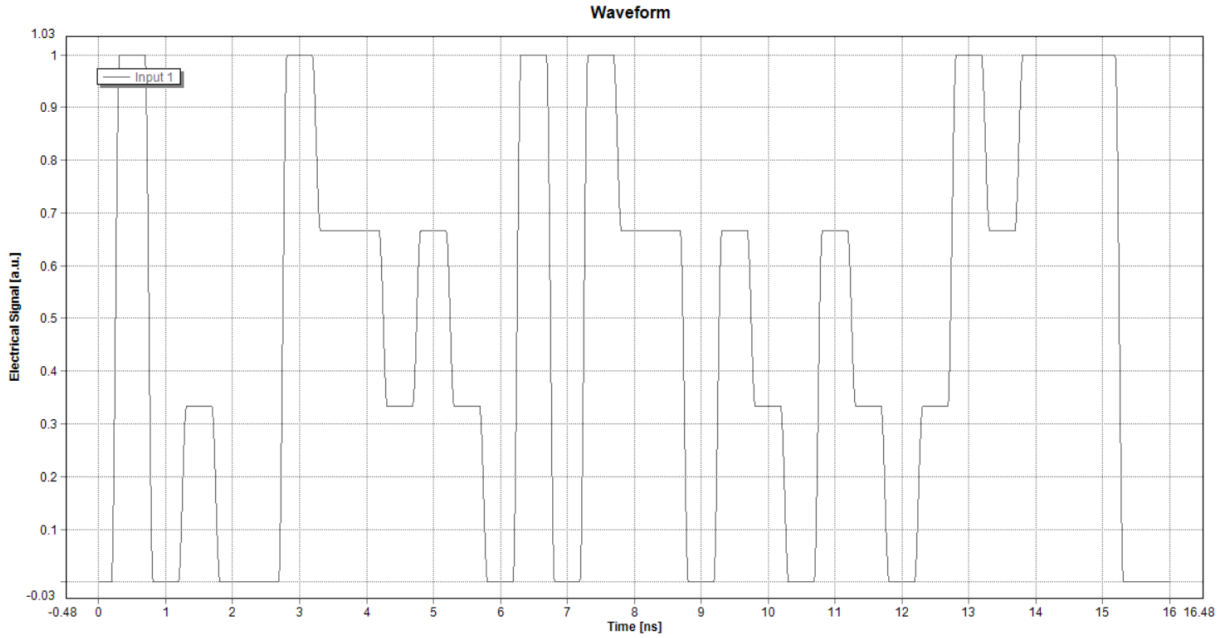


Figure 5.7 ePAM4 signal that drives the DML-EAM hybrid.

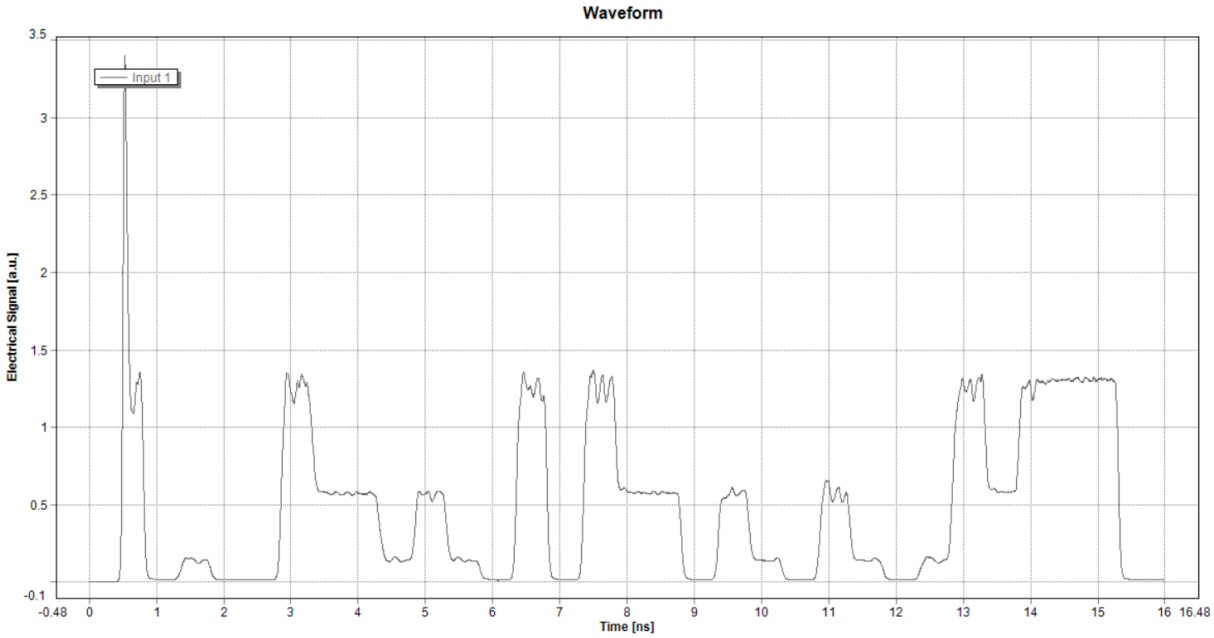


Figure 5.8 Generated oPAM4 signal from the DML-EAM Hybrid.

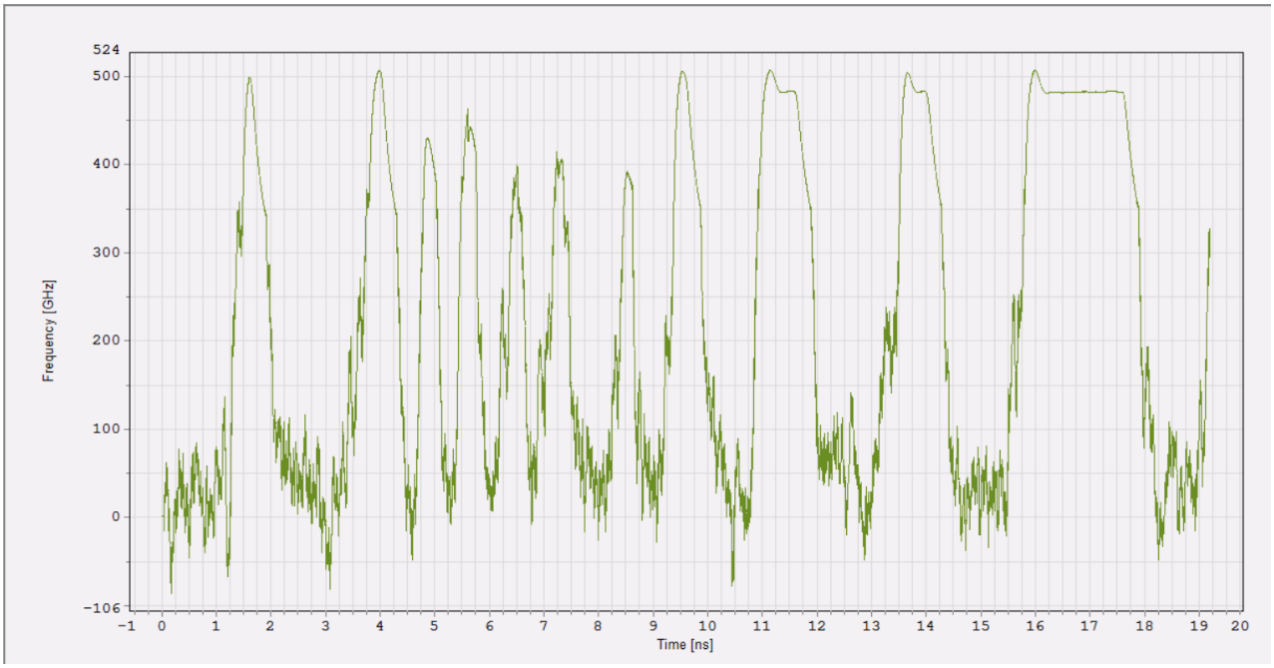


Figure 5.9 Generated PAM2 signal in case of DML.

As stated in [8] the major effect of DML is the associated phase modulation to the intensity modulation, which results in CD and then ISI. In the HM model, some degree of chirp is still present in the modulated signal, which introduces limitations. With the concept of chirp managed lasers (CML) through an optical signal reshaper (OSR), the transient chip from the DML can be reduced. The authors also includes a digital signal process for improving their received signal, all of whom did not discussed in the paper and so they we are not implemented.

5.3 IMPLEMENTATION OF SILICON PHOTONIC MODULATOR AND INTEGRATION IN NOVEL ODAC DESIGN

Different reasons make the adoption of Optical Digital to Analog Converters, eDAC free, to directly convert digital bit streams into multilevel PAM/QAM optical signals advantageous. These state-of-the-art oDACs are based on Segmented Mach Zehnder Modulators, based on multiple binary modulation segments, serially strung along the two MZM arms. There have been

multiple experimental demonstrations of two-segment SEMZM for PAM4 constellation generation for Direct Detection (DD) optical transmission links, as well as for *m*-QAM generation for Coherent (COH) detection, realized using a pair of IQ-nested multi-segment SEMZMs. As stated in [9] the segmented MZM design parameters are the peak phases induced in each of the electrode segments. The inspirations have come by the analogous modern eDAC electronic linear circuits and so the peak segment phases are typically designed to form a geometric sequence with ratio 2, ignoring the interferometric sine nonlinearity of combining the two SEMZM arms. For PAM4 DD SEMZMs, when equal voltages (lengths) are used for the two segments, the segment lengths (voltages) are taken in 2:1 respective ratio. Moreover, to mitigate the sine nonlinearity, substantial backoff (peak voltage below the π-voltage) is applied, degrading modulation efficiency. In reference 9 it is proven that these current PAM4 segmented MZM design practices are grossly suboptimal, and it presents that the DD PAM4 segmented MZM sine nonlinearity is an 'ally', enabling synthesis of a perfect regular staircase PAM4 oDAC characteristic, stretching the oDAC dynamic range out to its maximum full-scale. The optimization of [9] is implemented by means of simple modification of the photonic layout dimension, more specifically the modification of the ratio of electrodes lengths, accounting for the segment voltages. Moreover, a common design serves both PAM4 DD and PAM4 COH generation (PAM4 COH refers here to bipolar 4-level format for nesting I/Q tributaries in a 16QAM COH link). This design unlocks ~7 dB extra performance, hitherto untapped for PAM4 DD and for 16QAM. This boost arrives just-in-time to enable next-generation datacenter photonic interconnections

5.3.1 Serial Segmented MZM acting as oDAC for Direct Detection

In this section the verification of what is stated in [9] is going to be done, that is creating a 2 segment SEMZM and driving it with an NRZ signal a perfect optical PAM 4 is generated. Note that the work is based on the direct detect case and that the transfer function of a segmented MZM it doesn't significantly change from that of a simple MZM as the one descripted in section 5.1. So, for the case of segmented MZM the transfer function equals to:

$$Fc = sin[b1[c]\varphi 1 + b0[c]\varphi 2] \quad (38)$$

Similarly with the simply MZM the index labeling the OCs levels/codewords, ranges over {1,2,3,4} for a PAM4 OC. Naturallly, the argument of the sine in (1) models the phase accrual over the two modulation segments, which individually contribute phases

$$\varphi_s|_{s=1,2} \in \{0, {\varphi_1}^{pk}\} \quad (39)$$

for direct detection.

This lead to

$$F^{DD} = \{{F^{DD}}_1, {F^{DD}}_2, {F^{DD}}_3, {F^{DD}}_4\} = \{0, \sin({\varphi_0}^{pk}), \sin({\varphi_1}^{pk}), \sin({\varphi_1}^{pk} + {\varphi_0}^{pk})\} (40)$$

In reference 9 the authors begining from thess equations and solving a maximin problem give the solution for the perfect PAM 4 as

$${\varphi_1}^{pk} : {\varphi_0}^{pk} = \text{asin}\left(\sqrt{\frac{2}{3}}\right) : \text{asin}\left(\sqrt{\frac{1}{3}}\right) = 1.55:1 \qquad (41)$$

Now the L1,L2 the lengths required in the optimal design and both sealected at the π-switching voltage Vπ. The Vπ refers to a fictious MZM with electrode length equal to the sum of the two segments of the SEMZM, Lπ= L1+L2. Then ${\varphi_s}^{pk} = \frac{L_s \pi}{L_\pi 2}$,so L1:L2 = 1.55:1 . For the Vpi simulation an silicon MZM based on that of section 5.1 is chosen. But a second waveguide is added to the schematic (figure 5.10), to act as the second segment of different Length of the SEMZM. Now the phase shifter has the parameters of $Length1 = ratio * Length$ and $Length2 = Length$ for L1 and L2 . The variable Length is written as

$$Length = LengthP(ratio + 1) \quad (42)$$

LengthP refers to the total length theoritical symbolised as $L\pi$. Now the python script contains two different functions each for the waveguide with the respective Length. So

$$phase1(V) = -1 * (sgn) * (90) * (Length1/Lp) * (V/Vp) + sgn * 45 \quad (43)$$

$$phase2(V) = -1 * (sgn) * (90) * (Length2/Lp) * (V/Vp) + sgn * 45 \quad (44)$$

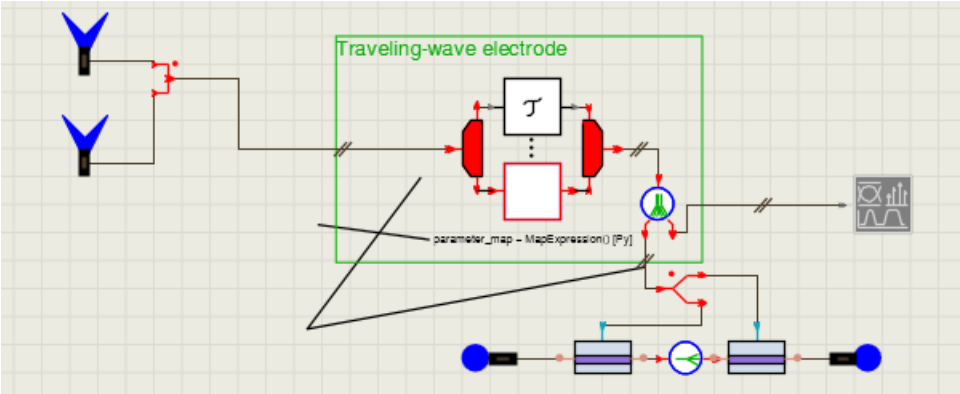


Figure 5.10 Phase shifter with two waveguides acting as different segments.

As previously explained the schematic of the MZM figure 5.11 produces the cosine fuction so the trigonometric equation of $\sin\theta = \cos(90 - \theta)$ must be used. In this case the phase propagates through two waveguides so the first adds the 45 degrees and the second one the rest.

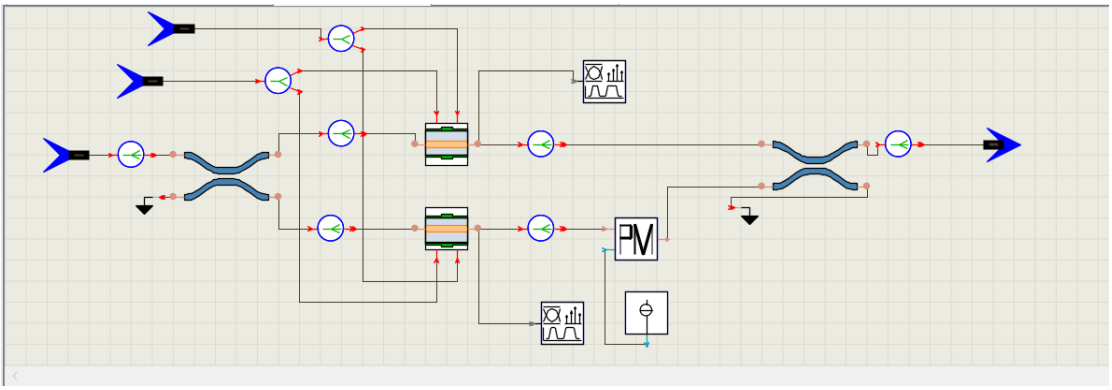


Figure 5.11 SEMZM that uses the phase shifter of Figure 5.10

Now that the segmented MZM is implemented a simulation to prove its operation is done by generating two-bit code words and driving the MSB in the upper electrical input of the SEMZM and the LSB to the lower Figure 5.12. Two generate those first a PRBS generator is used (first module of left side), then a module that creates a matrix of int-points is used as an input to the PAM mapper, the output of which is a matrix of PAM signal levels based on the input matrix. The fourth module states that the signal is an input signal, and the next module compiles the following python code:

```
import numpy as  np
def I_example(input,n):
   inputLength=input.shape;
   rowLength=inputLength[0];
   x=np.empty((rowLength,1));
   for i in range(0,rowLength):
      x[i,0]=input[i,n-1];
   return x
```

Then the bitstream is send to the two separate path of MSB and LSB , where the second module compiles the following python code:

```
import os;
import numpy;
from os import *;
from math import *;
'"from numpy import zeros, float;"'
def I_example(input):
        arrayLength=input.shape;
        rowsCount=arrayLength[0];
        output=numpy.empty((rowsCount,2));
        for i in range(0,rowsCount)
                if(input[i]== 0):
                        output[i,0]=0;
                        output[i,1]=0;
                if(input[i]== 1):
                        output[i,0]=0;
                        output[i,1]=1;
```

```
            if(input[i]== 2):
                output[i,0]=1;
                output[i,1]=0;
            if(input[i]== 3):
                output[i,0]=1;
                output[i,1]=1;
        return output.astype(int)
```

Next the signal travels through a DAC, that implements a transfer function in this case is unnecessary and then the electrical blocks are transformed into electrical samples for the waveguides, which are nested inside the SEMZM to work properly. The last module is the driver with DriveAmplitude equal 10V and before it is a rise time adjuster.

The optical eye diagram that is generated is a perfect PAM4 with equal spacing between its levels Figure 5.13.

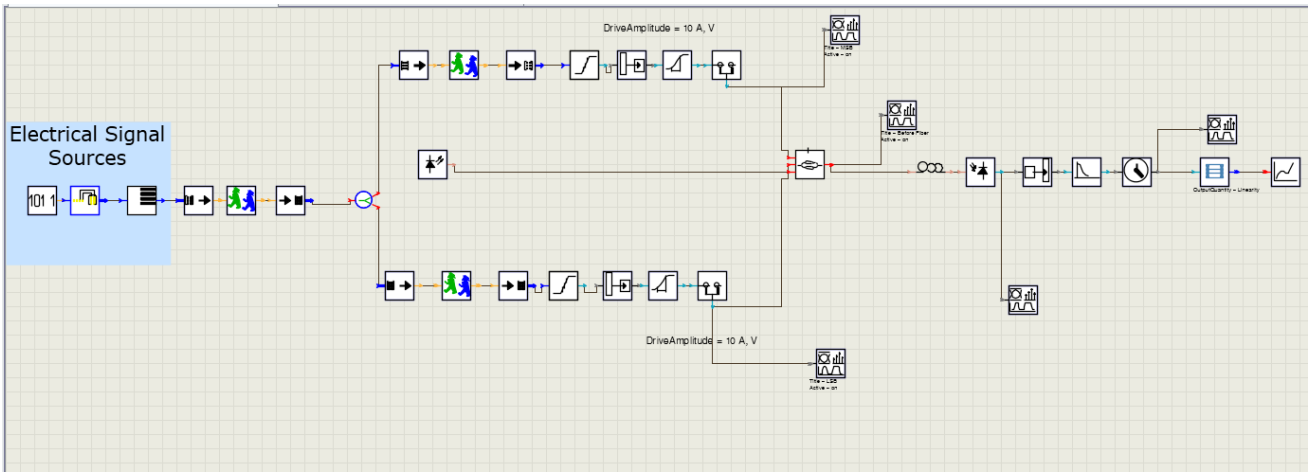


Figure 5.12 Schematic that simulates the operation of the SEMZM by driving MSB and LSB to each segment of the SEMZM

To further verify the theory that the ratio between the lengths of the two segments must be equal to 1.55 to produce a perfect PAM4, different ratios are tested. Eye diagrams of every

simulation is generating none with better performance than the proposed schematic. Between them is also the ratio of 2 , that everyone else uses.

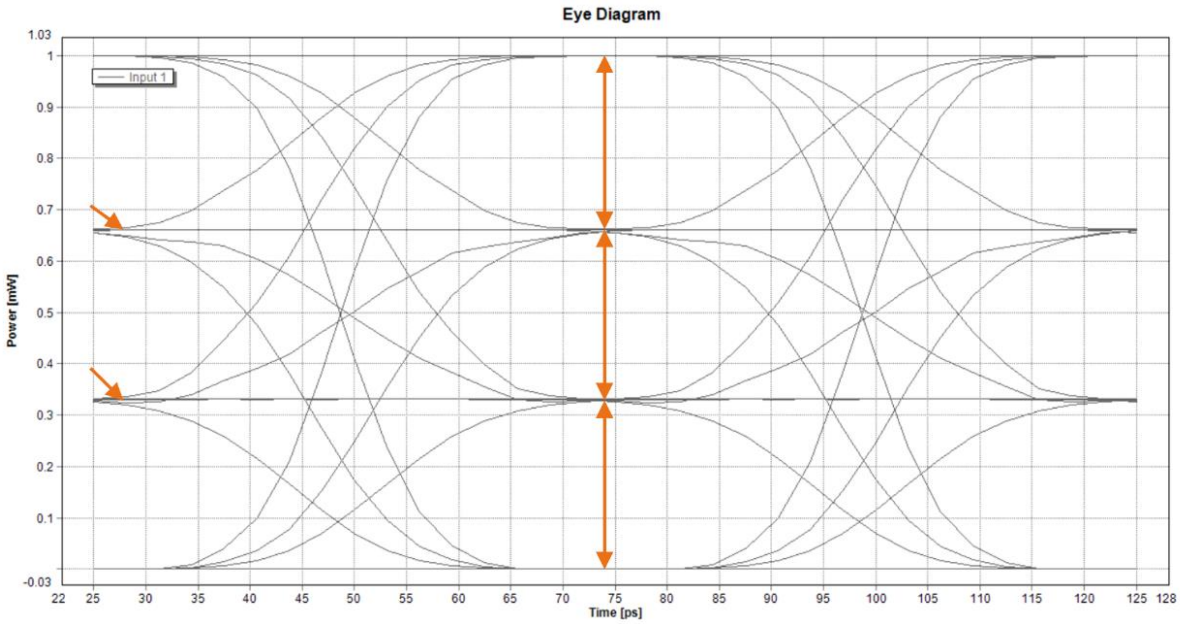


Figure 5.13 Eye diagram of the received pulse. The levels are equally spaced and are those of a 'perfect' PAM4

To further verify the theory that the ratio between the lengths of the two segments must be equal to 1.55 to produce a perfect PAM4, different ratios are tested. Eye diagrams of every simulation are generating none with better performance than the proposed schematic. Between them there is the ratio of 2, that everyone else uses.

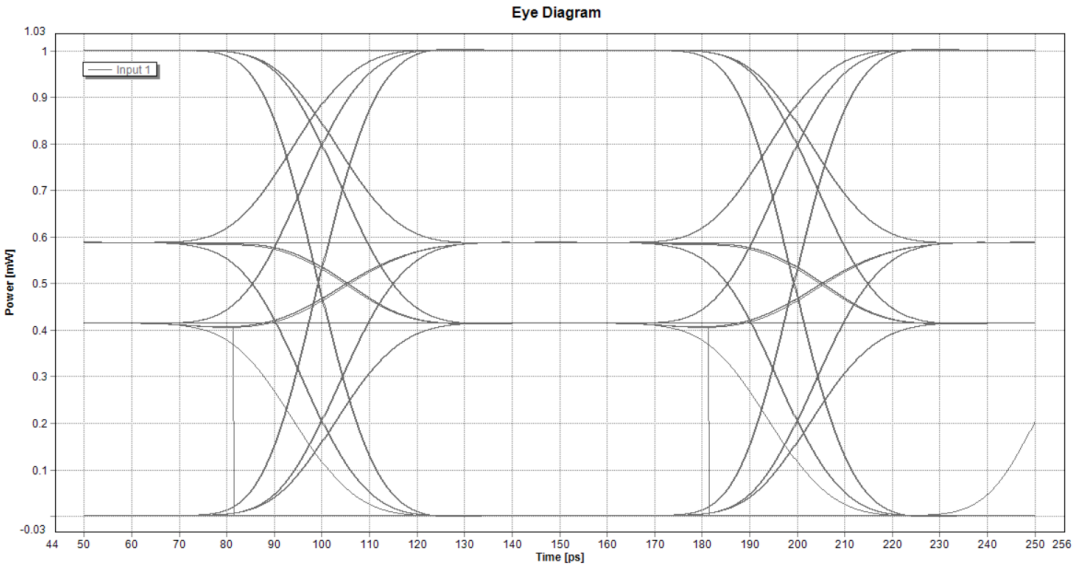


Figure 5.14 Received Eye Diagram in case that ratio ==1.25

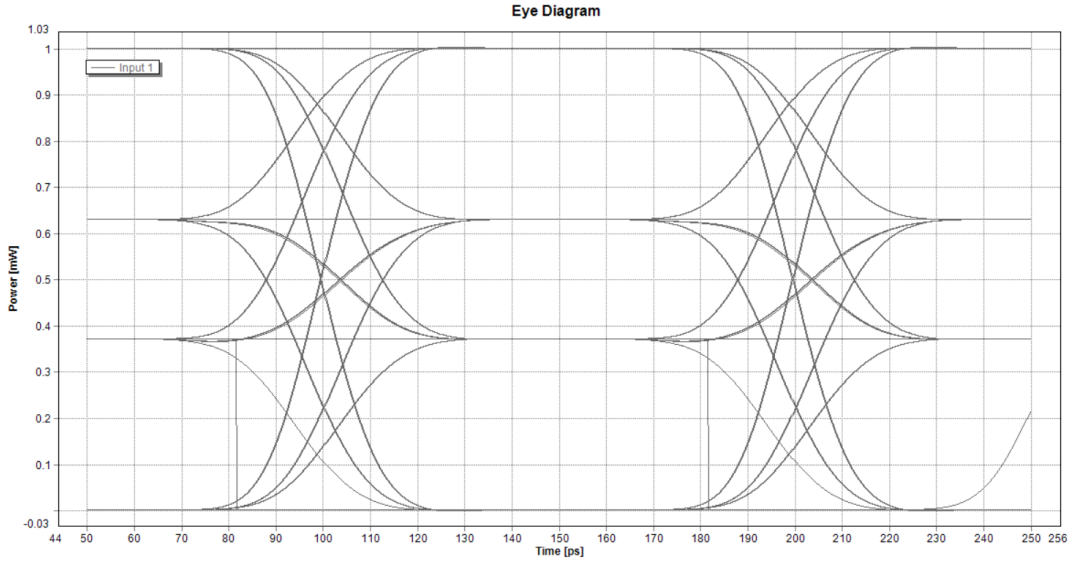


Figure 5.15 Received Eye Diagram in case that ratio == 1.4.

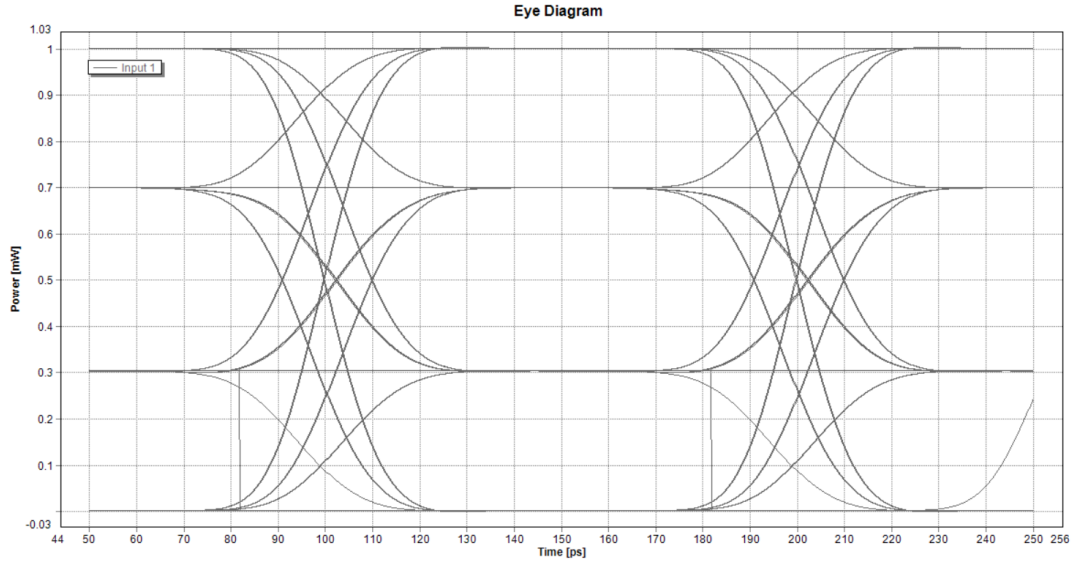


Figure 5.16 Received Eye Diagram in case that ratio ==1.7

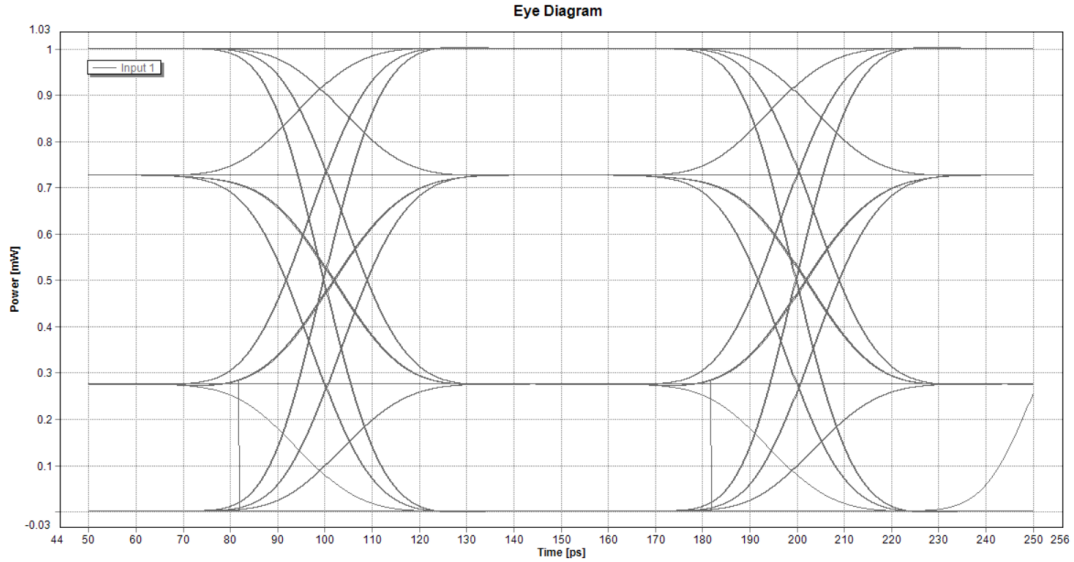


Figure 5.17 Received Eye Diagram in case that ratio == 1.85.

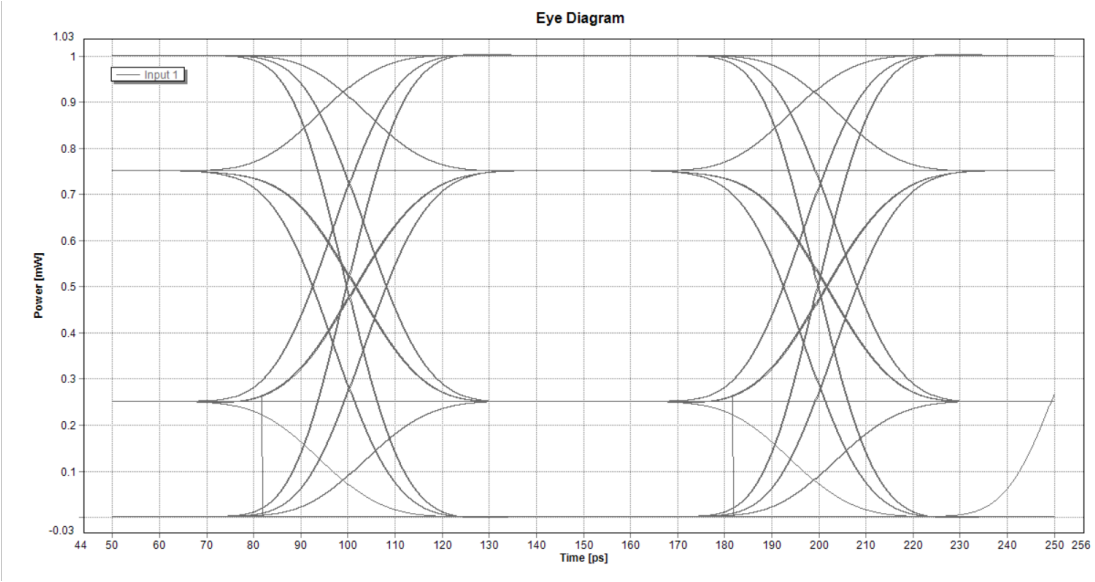


Figure 5.18 Received Eye Diagram in case that ratio == 2

Besides the visual distortion of the eye diagram, another way to verify the therotical conclusion of [9], is by introducing the coefficient of eye linearity. Eye linearity is a metric that is combined of average symbol levels. To measure eye linearity, first a horizonal mask about Tmid is plotted (Tmid is the center of 1e-6 BER contour for middle eye). Then the eye width is measured. Given the separations of the symbol levels AVlow = μ1-μ0 , AVmid = μ2-μ1 , AVupper = μ3-μ1, where μi is mean of level i, the eye linearity is the ratio

$$Linearity = \frac{\min(AVlow, AVmid, AVupper)}{\max(AVlow, AVmid, AVupper)}$$

The above eye diagrams have the following linearity

Ratio=1.25	Level 3	1	Aupp = 0.414	
	Level 2	0.586	Amid = 0.175	L= 0.175/0.414 = 0.422
	Level 1	0.411	Allow= 0.411	
	Level 0	0		

Table 8 Levels of PAM4 Constellation and Eye Diagram Linearity for ratio =1.25

Ratio=1.4	Level 3	1	Aupp = 0.37	
	Level 2	0.630	Amid = 0.259	L= 0.259/0.370= 0.7
	Level 1	0.371	Allow= 0.371	
	Level 0	0		

Table 9 Levels of PAM4 Constellation and Eye Diagram Linearity for ratio =1.4

Ratio=1.55	Level 3	1	Aupp = 0.333	
	Level 2	0.666	Amid = 0.333	L= 0.333/0.333 = 1
	Level 1	0.333	Allow= 0.333	
	Level 0	0		

Table 10 Levels of PAM4 Constellation and Eye Diagram Linearity for ratio =1.55

Ratio=1.7	Level 3	1	Aupp = 0.301	
	Level 2	0.699	Amid = 0.399	L= 0.300/0.399 = 0.75
	Level 1	0.3	Allow= 0.300	
	Level 0	0		

Table 11 Levels of PAM4 Constellation and Eye Diagram Linearity for ratio =1.7

Ratio=1.85	Level 3	1	Aupp = 0.275	
	Level 2	0.725	Amid = 0.45	L= 0.275/0.45 = 0.611
	Level 1	0.275	Allow= 0.275	
	Level 0	0		

Table 12 Levels of PAM4 Constellation and Eye Diagram Linearity for ratio =1.85

Ratio=2	Level 3	1	Aupp = 0.250	
	Level 2	0.750	Amid = 0.500	L= 0.25/0.5 = 0.5
	Level 1	0.250	Allow= 0.250	
	Level 0	0		

Table 13 Levels of PAM4 Constellation and Eye Diagram Linearity for ratio =2

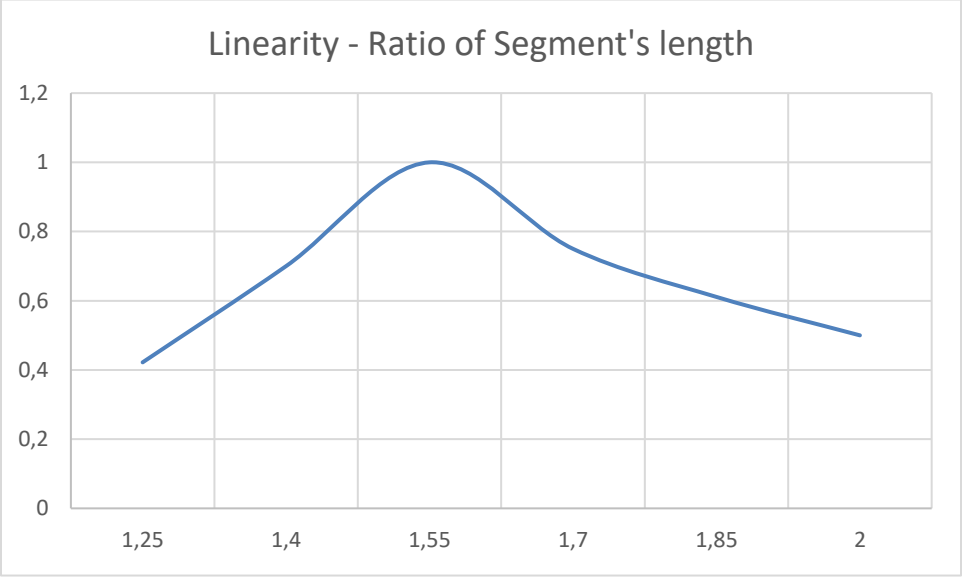


Figure 5.19 figure of linearity versus ratio between segment's length.

5.3.1 Serial Segmented MZM performing as oDAC for Coherent Detection

If the term 'perfect' COH PAM4 constellation is permitted, it will be descoping a max-full-scale equi-spaced bipolar[1] symmetric OC. $F^{COH} = [-1, -\frac{1}{3}, \frac{1}{3}, 1]$. To derive the PAM4 COH as a function of the phase design parameter the codewords must be substitute into

$$Fc = sin[b1[c]\varphi 1 + b0[c]\varphi 2] \quad (45)$$

[1] Bipolar PAM means that the 1D constellation comprise both positive and negative, in contrast with unipolar PAM-for-DD, having all its level non-negative.

yielding the following four field levels:

$$F^{COH} = \{F^{COH}{}_1, F^{COH}{}_2, F^{COH}{}_3, F^{COH}{}_4\} = \{\sin(-\varphi_1{}^{pk} - \varphi_0{}^{pk}), \sin(-\varphi_1{}^{pk} + \varphi_0{}^{pk})$$

$$sin(\varphi_1{}^{pk} - \varphi_0{}^{pk})\sin(\varphi_1{}^{pk} + \varphi_0{}^{pk})\}$$

$$F^{COH} = \{F^{COH}{}_1, F^{COH}{}_2, F^{COH}{}_3, F^{COH}{}_4\} = \{1, -\cos(2\,\varphi_0{}^{pk}), \cos(2\,\varphi_0{}^{pk}), 1\} \quad (46)$$

Surpisingly the same optimizer pahase paramete, $\varphi_0{}^{pk}$aas derived for DD PAM4 , also maximin-optimizes, yielding a 'perfect' COH PAM4 constellation :

$$F^{COH}(asin\sqrt{\tfrac{1}{3}}) = [-1, -\tfrac{1}{3}, \tfrac{1}{3}, 1] \quad (47)$$

In terms of Vpi implementation they are now significants changes, besides the fact that the drivers know driving both negative and positive amplitudes. And that the python code can now also take negative signals. So the LSB and MSB now swing between [-10, 10] where -10 represents the logical '0' and 10 the logical '1'. Now that the minus in phase can be produced the sign parameter is not needed but nothing else change , so the phase is

$$p1(V) = -1 * (90) * (Length1/Lp) * (V/Vp) + 45 \quad (48)$$

$$p2(V) = -1 * (90) * (Length2/Lp) * (V/Vp) + 45 \quad (49)$$

The images from vpi are :

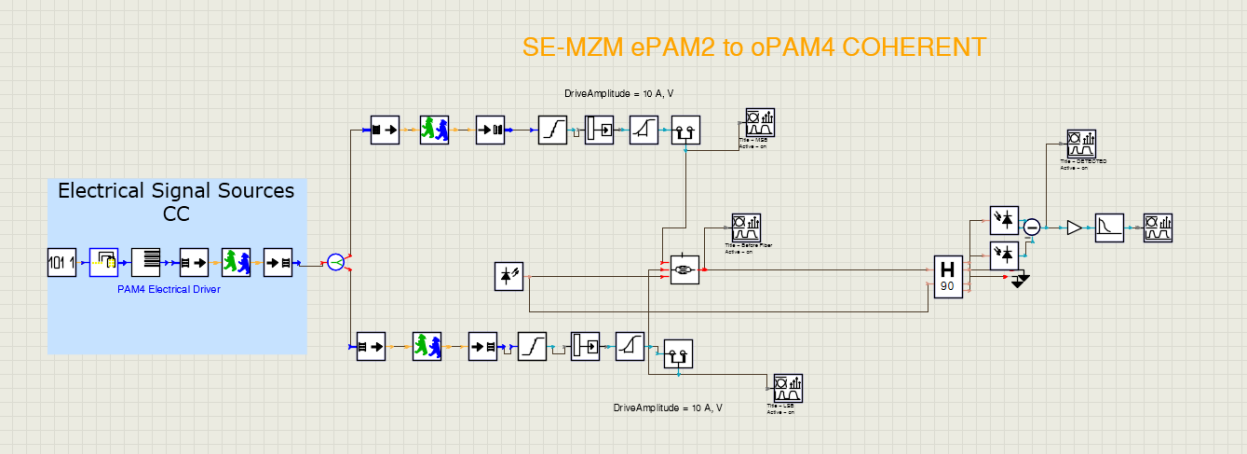


Figure 5.19 Transmission Simulation of SEMZM ePAM2 to oPAM4 bipolar coherent detection

As can be seen not many things have changed, other than the transfer function, so the 0 to be treated as -1 and the fact that a coherent received (left side after SEMZM) is required to detect

the signal . After the detection an amplifier of gain 100 and a bessel filter are used and the following signal is received.

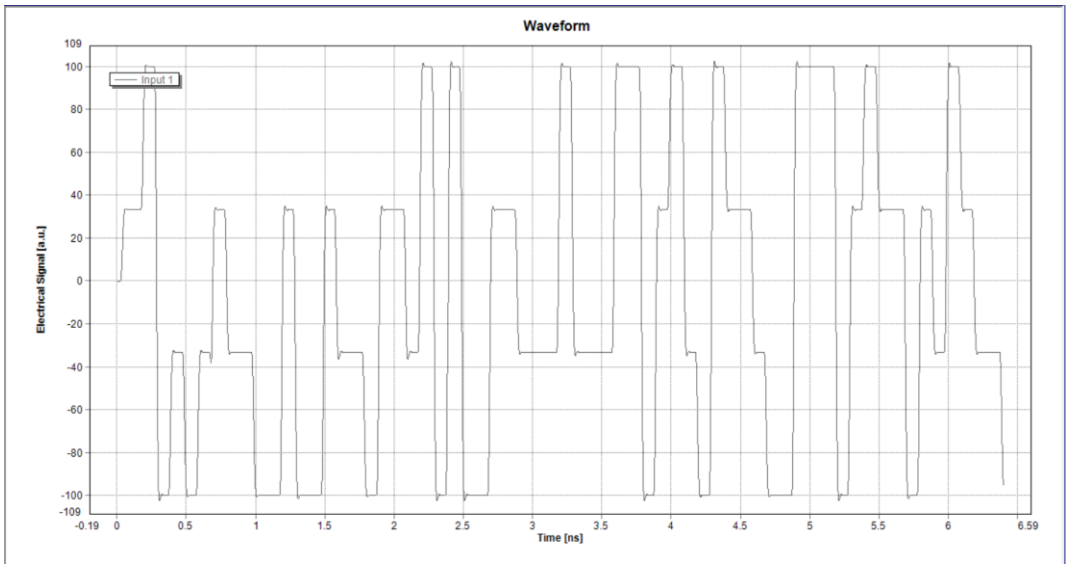


Figure 5.20 Received Optical PAM4 signal of the transmission schematic figure 5.19

The pulse in figure 5.20 is a 'perfect' COH PAM4 [-100, -100/3, 100/3 , 100]. And the same result can been seen in the eye diagram.

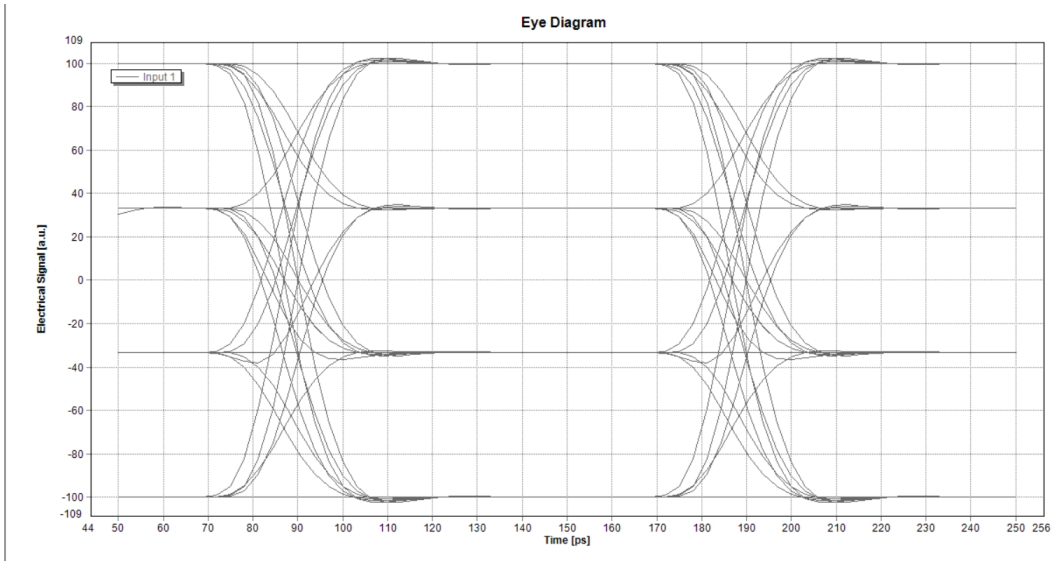


Figure 5.21 Perfect Bipolar PAM4 optical signal generated by the transmission schematic figure 5.19

5.4 IMPLEMENTATION OF PARALLEL ARCHITECTURE OF SEGMENTED MZM

In [10] a new optical PAM generation concept based on parallel MZM is presented. Starting from the most general S-way Multi-Level – Driven Multi-Parallel oDAC, the perfection in terms of performance can be seen. The novel ODAC architecture significantly improves the triple tradeoff between power consumption versus the constellation quality versus modulation rate. Moreover, the total complexity size and cost of the system is minimized due to the simpler electrical circuits that are required. The S-paths proposed novel oDAC structure depicted in figure 5.22 is composed by S parallel acting as gates, between 1:S optical splitter and an S:1 combiner.

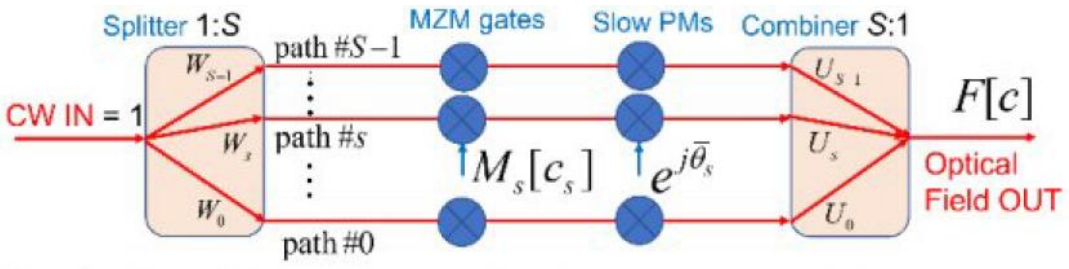


Figure 5.22 Schematic of S-way Multi-Level – Driven Multi-Parallel oDAC

Let the s-th MZM path have a modulation Transfer Factor (Tf)$M_s[c_s]$ with index c_s with index s$\in \{0,1,\dots,S-1\}$ labeling the paths and $c_s \in \{0,1,\dots,C_s\}$ labeling the modulation levels of each MZM. The s-th MZM generates C_s optical levels, as it can be driven by $C_s - PAM$. ThusC_s is also the size of the multilevel Epam constellation driving the s-path MZM Optical gate, and c_s the codework respectively. The TF levels of each MZM are designed such as to attain an optimal field constellation $F \equiv \{F[c]\}_{c=1}^{cs}$ at the oDAC output, of constellation order $C = \prod_{s=1}^{s} C_s$. The slow moving-average modulation TF of the s-th path is given by $e^{j\theta_s}, s = 0,1,\dots,S-1$ with θ_s the total slow phase in the s-th path. The 1:S splitter has power splitting ratio $W_s, \mu\varepsilon \sum_{s=0}^{s=1} W_s = 1$, The S:1 combiner has power combining ratio U_s, $s.t. \sum_{s=0}^{s=1} U_s = 1$, The respective field split and

combine ideal ratios are $\sqrt{\mathrm{W_s}}$, $\sqrt{\mathrm{U_s}}$. The I/O output constellation (for unit amplitude optical input) F[c] = F[$c_0, c_1, \dots, c_{s-1}$] is

$$\mathrm{F[c]} = \sum_{s=0}^{S-1} \sqrt{A^{sph} W_S}\, M_s[c_s] \sqrt{A^{path}} e^{j\theta s} \sqrt{A^{cmb} U_s} = \sqrt{A^{xcss}} \sum_{s=0}^{S-1} \sqrt{W_s}\, M_s[c_s] e^{j\theta s} \sqrt{U_s} \quad (50)$$

With $A^{xcss} \equiv A^{path} A^{splt} A^{cmb}$. Without loss of generality considering a free of excess loss oDAC with equalized phase shift in all paths leads to setting $A^{xcss} = 1$ and θs = 0. And a matches spilt- combine ratio F[c] = F[$c_0, c_1, \dots, c_{s-1}$] =$\sum_{s=0}^{s=1} \mathrm{W_s} M_s[c_s]$ (51). Specializing this equation for S=2, yields the oDAC output levels:$F[C] = F[c0, c1] \in F \equiv [F^1, F^2, \dots, F^C]$ (60)

The oDAC output levels are obtained as linear combinations of all possible pairs of MZM field levels $Ms[c0] \in Ms \equiv [Ms^1, Ms^2, \dots, Ms^C]$ (61), to be plugged into the two-paths interferometric superposition , $F[c0, c1] = W0M0[c0] + W1M1[c1]$. The later equation is expressed as $F = W0M0 \oplus W1M1$, with the use of 'Kronecker sum'. Pluging an electrical PAM[2|4|8] in the later and as well W1 = 1- W0 yields

$$F = W0P * AMcoh[2|4|8] \oplus (1 - W0) * PAMcoh[2|4|8] \quad (62)$$

In [10] the following optimal analytic design is presented

$$PAM_{COH}[4] = \frac{1}{3} PAM_{COH}[2] \oplus \frac{4}{3} PAM_{COH}[2]$$

$$PAM_{COH}[8] = \frac{1}{7} PAM_{COH}[2] \oplus \frac{6}{7} PAM_{COH}[4]$$

$$PAM_{COH}[8] = \frac{3}{7} PAM_{COH}[4] \oplus \frac{4}{7} PAM_{COH}[2]$$

$$PAM_{COH}[16] = \frac{1}{5} PAM_{COH}[4] \oplus \frac{4}{7} PAM_{COH}[4]$$

$$PAM_{COH}[16] = \frac{1}{15} PAM_{COH}[8] \oplus \frac{8}{15} PAM_{COH}[2]$$

$$PAM_{COH}[16] = \frac{1}{15} PAM_{COH}[2] \oplus \frac{14}{15} PAM_{COH}[8]$$

This multi-parallel multi-level novel architecture for an o-DAC analysis act as the bases of the suggested model of this section. The combination of 2 segments Segmented-MZM in two paths parallel oDAC architecture is suggested. This will enable to have the advantage of the parallel architecture and farther improve the characteristics of the system with using lower order electronics reducing complexity and cost and smaller in length segments allowing for bigger bandwidth. In the studied and implemented case an PAM2 of 4 bits per symbol is used to drive its segmented of the parallel- segmented MZM oDAC respectively. The final result is a 'perfect' PAM16 COH.

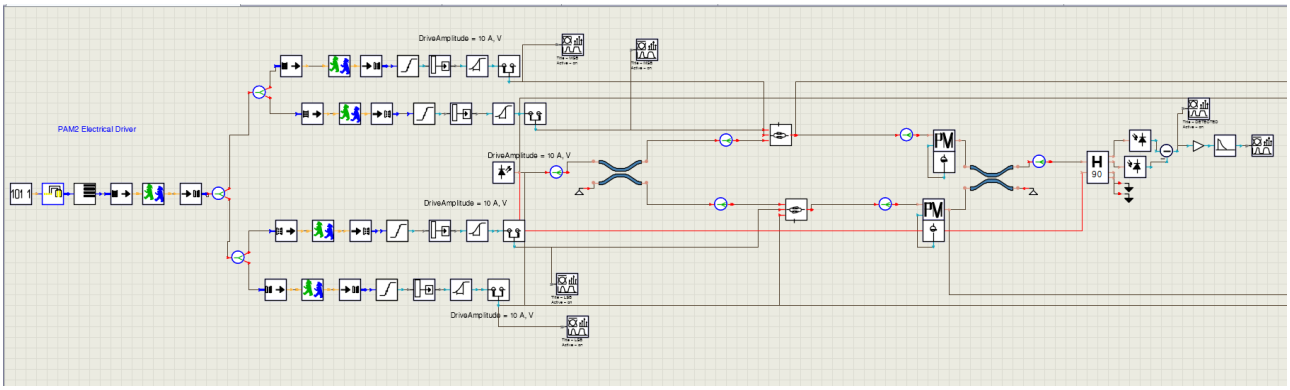


Figure 5.23 Transmission schematic of parallel oDAC with SEMZM in each arm

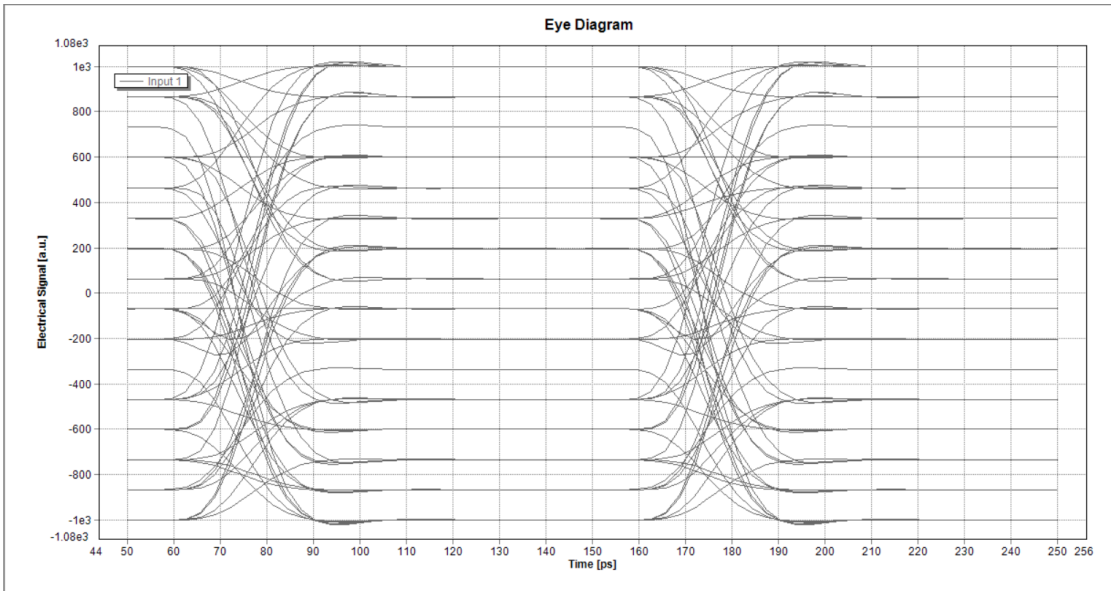


Figure 5.24 Perfect Bipolar PAM 16 optical signal received after the oDAC figure 5.23

CONCLUSIONS

This thesis has presented all the contemporary platforms of modulators. Starting from the electro-optic effects and continuing with the topologies, the concept of the modulator can be understood. Next the basic materials and fabrication techniques have been presented so that the modulators can now be seen as real-world devices with drawbacks and advantages. Their limitations and capabilities have been explained. Finally, the implementation of the oDAC has been carried out in the last chapter and it can now be understood that the performance needed in the next generation of transmission system can be achieved with the combination of ultra-fast devices and better architecture. In the case of the segmented modulation the shrinking of the segment's length leads to wider bandwidth. The overall use of as simple as possible electrical devices reduces the cost, ensures energy efficiency, and minimizes complexity of the system as a whole. But most importantly the devices' design allows for a perfect constellation, meaning lower BER and less requirements for digital signal processing.

REFERENCES

1. S.O. Kasap ,(2001) Principles of Electronic Materials and Devices.
2. Georgios Sinatkas, Thomas Christopoulos, Odysseas Tsilipakos, Emmanouil E. Kriezis,(2021), Electro-Optic modulation in integrated photonics
3. JACOB SCHEUER, WILLIAM M.J. GREEN AND AMNON YARIV (2022, November,25) retrieved https://www.photonics.com/Articles/Annular_Bragg_Resonators_Beyond_the_Limits_of/a21871
4. SYNOPSYS retrieved https://www.synopsys.com/photonic-solutions/product-applications/foundry-process-tw-mzm.html
5. Wei Shi, Yelong Xu, Hassan Sepehrian, Sophie LaRochelle, and Leslie A. Rusch, (2018), Silicon photonic modulators for PAM transmissions (Volume 20, Issue 8)\
6. Ansheng Liu1, Ling Liao1, Doron Rubin2, Hat Nguyen1, Berkehan Ciftcioglu1, Yoel Chetrit, Nahum Izhaky, and Mario Paniccia1, (2007) ,High-speed optical modulation based on carrier depletion in a silicon waveguide
7. Changhao Han, Ming Jin , Yuansheng Tao 1, Bitao Shen 1, Haowen Shu 1, and Xingjun Wang (2022), Ultra-compact silicon modulator with 110 GHz bandwidth, Optical Publishing Group 2022
8. Adebayo E. Abejide, Madhava R. Kota, Sushma Pandey, Oluyomi Aboderin, Cátia Pinho, Mário Lima and António Teixeira, (2022), Direct and External Hybrid Modulation Approaches for Access Networks

9. Moshe Nazarathy, Ioannis Tomkos (2021) 'Perfect' PAM4 serial digital-optical conversion

10. Moshe Nazarathy, and Ioannis Tomkos (2021) Accurate Power-Efficient Format-Scalable Multi-Parallel Optical Digital-to-Analogue Conversion

11. Jörn P. Epping1, Denys Marchenko1, Arne Leinse1, Richard Mateman1, Marcel Hoekman, Lennart Wevers1, Chris G. H. Roeloffzen1, Matthijn Dekkers2, and René G. Heideman (2020), Ultra-low-power stress-based integrated photonic phase actuator